

ARTICLE TYPE

Reduced-Gate Convolutional LSTM Using Predictive Coding for Spatiotemporal Prediction

Nelly Elsayed*¹ | Anthony S. Maida² | Magdy Bayoumi²¹School of Information Technology,
University of Cincinnati, Ohio, USA²School of Computing and Informatics,
University of Louisiana at Lafayette,
Louisiana, USA**Correspondence**

*Nelly Elsayed, Email: nelly.elsayed@uc.edu

Summary

Spatiotemporal sequence prediction is an important problem in deep learning. We study next-frame(s) video prediction using a deep-learning-based predictive coding framework that uses convolutional, long short-term memory (convLSTM) modules. We introduce a novel reduced-gate convolutional LSTM (rgcLSTM) architecture that requires a significantly lower parameter budget than a comparable convLSTM. By using a single multi-function gate, our reduced-gate model achieves equal or better next-frame(s) prediction accuracy than the original convolutional LSTM while using a smaller parameter budget, thereby reducing training time and memory requirements. We tested our reduced gate modules within a predictive coding architecture on the moving MNIST and KITTI datasets. We found that our reduced-gate model has a significant reduction of approximately 40 percent of the total number of training parameters and a 25 percent reduction in elapsed training time in comparison with the standard convolutional LSTM model. The performance accuracy of the new model was also improved. This makes our model more attractive for hardware implementation, especially on small devices. We also explored a space of twenty different gated architectures to get insight into how our rgcLSTM fits into that space.

KEYWORDS:

rgcLSTM, convolutional LSTM, convLSTM, predictive coding, spatiotemporal prediction, video prediction

1 | INTRODUCTION

The brain in part acquires representations by using learning mechanisms that are triggered by prediction errors when processing sensory input^{1,2,3}. An early implementation using this approach is by Rao et al.³ to model non-classical receptive field properties in the neocortex. The hypothesized brain mechanisms underlying this “predictive coding” are based on the concept of bi-directional interactions between the higher and lower-level areas of the visual cortex. The higher-level areas send predictions about the incoming sensory input to the lower-level areas. The lower-level areas compare the predictions with ground truth sensory input and calculate the prediction errors. These are in turn forwarded to the higher-level areas to update their predictive representations in light of the new input information.

Lotter et al.⁴ introduced a predictive coding architecture to the deep learning community. Specifically, they introduced PredNet for next-frame video prediction. The architecture was based on a deep neural-network framework that used a hierarchy of convolutional LSTMs. Since it was a deep network, it could readily be implemented and studied using off-the-shelf deep learning

⁰**Abbreviations:** rgcLSTM, reduced-gate convolutional LSTM; LSTM, long short-term memory

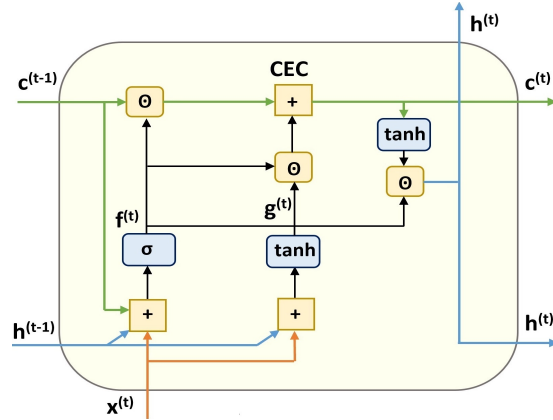


FIGURE 1 Diagram of an unrolled rgcLSTM cell. The single module gate, f , sends information to three locations which correspond to the output values of the forget, input, and output gates of the standard LSTM.

frameworks (e.g., Keras⁵, PyTorch⁶, TensorFlow⁷). This was in contrast to earlier predictive coding models¹ with a primarily mathematical formulation that offered little or no implementation guidance.

One of the main module types within the PredNet architecture is the representation module which is implemented as a basic convolutional LSTM (cLSTM). The module, when coupled with other modules, supports gated recurrent processing of video sequences and is trained to anticipate, or predict, the next frame that will appear in the sequence.

Our work replaces the cLSTM modules within the Lotter et al.⁴ model with a gated convolutional network that has fewer parameters. Its distinguishing feature is that it uses a single gate to perform three different functions. We call this the reduced-gate convolutional network, or “rgcLSTM” which introduces the concept of multi-function gates. The single gate uses shared weights to perform three functions and we classify it as a *multi-function gate model*. This allows a gate to perform more than one traditional function, thereby reducing the number of needed gates and the associated parameter count. Because of its smaller parameter budget, the rgcLSTM has a smaller memory footprint and faster training while maintaining or improving the prediction performance accuracy of the original model.

The present paper motivates and evaluates the design of our rgcLSTM, shown in Figure 1, whose novel features are the use of convolution-based peephole connections and the single multi-function gate that serves the function of three gates, namely, the forget gate, the input gate, and the output gate. We present performance results on the moving MNIST (gray-scale) and KITTI traffic (RGB) dataset benchmarks with, and without, these modifications. We find that our architecture gives better next-frame(s) prediction accuracy on these datasets while using a smaller parameter budget in comparison to the original Shi et al.⁸ convLSTM. We also explore a space of twenty different gated RNN designs involving both multi-function and single-function gates. This enriches our insight into how these gated networks perform.

2 | BACKGROUND AND RELATED WORK

Recurrent neural networks (RNNs) process sequential data such as occurs in signal processing⁹, weather feeds¹⁰, time series¹¹, and videos^{4,8}. Spatiotemporal datasets such as video are sequential datasets where the sequence elements are images. Spatiotemporal prediction (e.g., video prediction) is a challenge that has received intense interest in deep learning over the last few years. Spatiotemporal prediction and video frame prediction typically use unsupervised learning^{12,8,4,13}. However, the models all use complicated architectures and a large parameter budget.

The module that we modify uses convolutional LSTM modules. LSTM modules are recurrent neural networks (RNNs) which have three gating mechanisms. Plain RNNs do not have gating mechanisms and suffer from vanishing and/or exploding gradient problems. Although, they can learn local sequential dependencies, the gradient issues prevent them from learning long-term dependencies.

The long short-term memory (LSTM) network, first introduced by Hochreiter and Schmidhuber¹⁴, was the first gated RNN recurrent unit design to mitigate the vanishing and/or exploding gradient problems and improve learning of long-term dependencies. The LSTM was a recurrent block, or cell, with considerable internal structure similar to that in Figure 2(b), which displays a

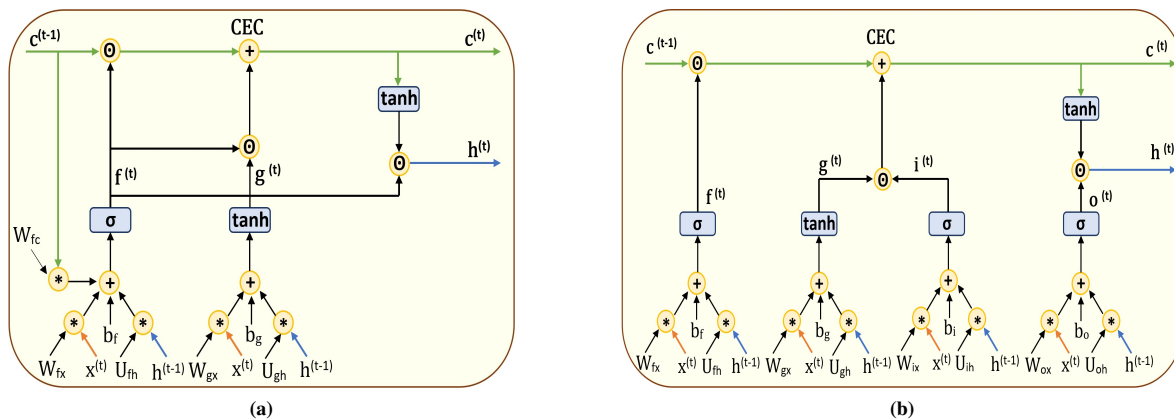


FIGURE 2 An operational diagram to make the trainable weights and biases explicit, along with their arithmetic operations, for the (a) rgcLSTM; and (b) cLSTM cell architectures. The proposed rgcLSTM has approximately 40% fewer trainable parameters than the cLSTM.

convolutional LSTM cell. Modern LSTMs have three gates and an input-update assembly. The gate names are “forget,” “input”, and “output”. To support learning, these gates employ trainable weights which are affine multiplied with the relevant gate input and then added to a trainable bias.¹⁵ This lets the data streams within the cell learn to remember or forget past information that is relevant or irrelevant to the task at hand for the current point in the data stream. Hochreiter and Schmidhuber¹⁴ introduced a second innovation to specifically address the vanishing/exploding gradient problems. They replaced the multiplicative transfer to previous states by additive transfer (indicated by the plus in the c line of Figure 1). The component to implement this was called the constant error carousel (CEC). Although mitigating the vanishing/exploding gradient problems, the CEC introduced a weakness into the LSTM design that became apparent when the output gate was closed. In this situation, the CEC could no longer affect the function of the input and forget gates (because the h inputs are cut off, as seen in Figure 2(b)). This problem was handled by adding peephole connections from the memory cell-state data line to each of the LSTM gates. This, however, comes at a cost of increasing the number of trainable parameters and associated overhead such as training time and memory footprint. For the rgcLSTM, only one peephole connection is needed. It goes from the cell state to the net input of the forget gate (see Figure 1 and Figure 2(a)).

There were attempts to design gated models to reduce the gate count while preserving learning power. Cho et al.¹⁶ proposed a gated recurrent unit (GRU) model. Instead of three gates, it used two: an update gate and a reset gate. The update gate combined the input gate, forget gate¹⁵. Thus, this is the first multi-function gate model. The reset gate served as the output gate of the LSTM cell¹⁵. This GRU model eliminated the output activation function and memory unit, but retained CEC¹⁵. The GRU yielded a reduction in trainable parameters compared with the standard LSTM. Zhou et al.¹⁷ used a single gate recurrent model called a minimal gated unit (MGU). Both models reduced the number of trainable parameters and gave results comparable to the LSTM¹⁸. There was a study based on the LSTM model in¹⁹ to examine the role and significance of each gate in the LSTM^{20,21}. This study showed that the most significant gate in the LSTM was the forget gate. However, it also showed that the forget gate needs other support to enhance its performance.

While the above gated RNNs are designed to process non-spatial sequential data, they must be augmented somehow to process spatiotemporal data. Shi et al.⁸ proposed a convolutional LSTM to enhance performance for spatiotemporal prediction, which we henceforth call the convLSTM to distinguish between the Lotter et al.⁴ cLSTM. The convLSTM operated on sequences of images. It had three gates characteristic of the regular LSTM, as well as elementwise peephole connections. The cLSTM was the same as the convLSTM, but without the peephole connections. Both models replaced the matrix multiplications (affine transformations) by convolutional operations for the input and recurrent input of each gate. The model achieved higher accuracy in comparison to the classical LSTM model. However, the number of parameters remained higher because the peephole connections still used elementwise multiplication. In recent research, Lotter et al.⁴ showed how to build the first predictive coding model using a simpler version of the convLSTM architecture which we call the cLSTM. The cLSTM had three gates but no peephole connections. The model achieved significant improvement in a predictive model as it did not need an encoder and decoder⁴. However, the number of parameters was large and grew linearly with the number of layers in the model.

There were other attempts to design smaller recurrent gated models based on the standard LSTM. They were based on either removing one of the gates or the activation functions from the standard LSTM unit. Empirical analysis¹⁵ compared these models and the standard LSTM. The conclusion found in Greff et al.¹⁵ was that these models had no significant improvement in either performance or training time. Moreover, these models had no significant reduction in trainable parameters. This empirical analysis¹⁵ also stated that the critical components of the LSTM model were the forget gate and the output activation function.

Our new gated model is named the *reduced-gate, convolutional LSTM* (rgcLSTM). Based on the empirical results of Greff et al.¹⁵, our model preserves the critical components of the LSTM while removing parameter redundancy. We use our model within a predictive coding framework introduced by Lotter et al.⁴ as a state-of-the-art approach for spatiotemporal prediction. The Lotter et al.⁴ model uses standard convLSTM modules (no peephole connections) within their predictive coding architecture. We replace those modules with our rgcLSTM. Our model shows a prediction accuracy comparable to the Lotter et al.⁴ design. However, our rgcLSTM reduces the number of trainable parameters and memory requirements by about 40% and the training time by 25% which makes it more attractive for hardware implementation on low power devices.

3 | REDUCED-GATE CONVOLUTIONAL LSTM ARCHITECTURE

The proposed rgcLSTM cell design appears in Figures 1 and 2(a). Figure 2 compares the proposed rgcLSTM and cLSTM architectures in enough detail for meaningful comparison of the arithmetic operations.

The rgcLSTM architecture has one trainable gated unit which we call the forget gate or module gate. Because of its inputs, it is comparable to an LSTM forget gate, but since it is the only gate in the module it also makes sense to call it the module gate. The model also preserves the cell memory state and retains the CEC to avoid vanishing and/or exploding gradients. There is a peephole connection from the cell state to the module gate but we have converted its operator from elementwise multiplication to convolution. This reduces the learning capacity of the rgcLSTM in comparison to a full LSTM with elementwise peephole connections to projecting all three gates. However, it still preserves information needed to allow the memory state to exert control over the module gate. It also helps the model extract features. Also, our model retains the output activation function. Thus, our model preserves the critical components of the LSTM as stated by Greff et al.¹⁵ while removing much of the parameter redundancy in the LSTM unit. This provides a significant reduction in the needed number of trainable parameters. Also, experiments in this paper show that our rgcLSTM model preserves the Lotter et al.⁴ model's prediction accuracy results.

The following describes the operation of the rgcLSTM depicted in Figure 2(a). We start by characterizing the forget gate. a^t denotes the net input to the forget/module gate activation function $\sigma(\cdot)$. Its value is calculated using the formula below.

$$a^t = [W_{fx}, U_{fh}, W_{fc}] * [x^{(t)}, h^{(t-1)}, c^{(t-1)}] + b_f \quad (1)$$

a^t is an $\eta \times \nu$ image with n channels. The square brackets on the righthand side of the equation are a channel-stacking operator and the "*" symbol denotes 'same' convolution. $x^{(t)}$ denotes the current multi-channel image input to the module. Its dimensions are $\eta \times \nu$ with γ channels. $h^{(t-1)}$ denotes the output of the cell from the previous time step and $c^{(t-1)}$ denotes the cell state from the previous time step. c and h have the same dimensions and number of channels as a . W_{fx} , U_{fh} , and W_{fc} are $m \times m$ convolution kernels to go with the cell inputs $x^{(t)}$, $h^{(t-1)}$, and $c^{(t-1)}$. W_{fx} has γ channels and U_{fh} and W_{fc} each have κ channels. W_{fc} implements the convolutional peephole connection. To match the output channel size for a , the following constraint is enforced: $\nu = \gamma + 2\kappa$. All three weight sets and biases b_f are trainable. To condense the notation we let $W_f = [W_{fx}, U_{fh}, W_{fc}]$ and $I_f = [x^{(t)}, h^{(t-1)}, c^{(t-1)}]$. Bias b_f is an n -element vector and is added to the appropriate image channel by broadcasting.

Note that the convolution operation between W_{fc} and $c^{(t-1)}$ implements the peephole connection and represents a departure from Shi et al.⁸ where an elementwise multiply was used (in contrast to a convolution operation in our model).

The total number of trainable parameters for the module gate is:

$$f_{\text{gate}}^{\#} = (m^2(\gamma + 2\kappa) + 1) \cdot n. \quad (2)$$

where the superscript "#" is a tag to indicate number of parameters. m^2 is the number of filter weights. $\gamma + 2\kappa$ is the number of input channels. n is the number of filters.

The module gate image value, $f_{\text{gate}}^{(t)} \in \mathbb{R}^{\eta \times \nu \times n}$, is obtained by applying a pixelwise activation function G to the net input image using

$$f_{\text{gate}}^{(t)} = G(a^t). \quad (3)$$

TABLE 1 Feature comparison between rgcLSTM, cLSTM and convLSTM cells.

Component	rgcLSTM	cLSTM	convLSTM
Number of gates.	1	3	3
Number of non-gate activation functions (tanh).	2	2	2
Has peephole connection?	Yes	No	Yes
Number of convolution kernels.	5	8	8
Number of non-convolutional weight matrices.	0	0	3
Number of elementwise multiplications.	3	3	6
Number of convolutional multiplications.	5	8	8
Number of bias vectors.	2	4	4

Depending on the application, G can be either the logistic (σ) or hard sigmoid (*hardSig*) function²². The pixel values of $f^{(t)}$ will fall in the range (0, 1) or [0, 1], depending on which function is used. Using σ , the gate value $f^{(t)}$ is calculated by:

$$f^{(t)} = \sigma(W_f * I_f + b_f). \quad (4)$$

Stacking makes the learning process more powerful than the non-stacked weights due to the influence of the x^t , $h^{(t-1)}$ and $c^{(t)}$ across convolutional weight set. Lotter et al.⁴ and Heck et al.²⁰ show empirically that stacking the input for recurrent units achieves better results than non-stacked input.

The input update (memory activation) uses a similar equation as for the module gate.

$$g^{(t)} = \tanh(W_g * I_g + b_g) \quad (5)$$

In the above, $W_g = [W_{gx}, U_{gh}] \in \mathbb{R}^{m \times m \times (\gamma + \kappa) \times n}$, and $I_g = [x^{(t)}, h^{(t-1)}] \in \mathbb{R}^{\eta \times \nu \times (\gamma + \kappa)}$. The number of channels in W_g is matching the number of channels of the W_f which make them computationally compatible. This approach is taken so that the dimension of $g_{\text{gate}}^{(t)} \in \mathbb{R}^{\eta \times \nu \times n}$ matches the dimension of $f_{\text{gate}}^{(t)}$. Similarly, the dimension of $b_g \in \mathbb{R}^{n \times 1}$ matches that of $b_f \in \mathbb{R}^{n \times 1}$. Finally, the number of trainable parameters for the input update is:

$$g_{\text{update}}^{\#} = (m^2(\gamma + \kappa) + 1) \cdot n. \quad (6)$$

Eqns. 2 and 6 count the total number of trainable parameters for the rgcLSTM cell. Eqn. 6 differs from Eqn 2 because the former does not have peephole connections. The total rgcLSTM parameter count is

$$\text{rgcLSTM}_{\text{cell}}^{\#} = f_{\text{gate}}^{\#} + g_{\text{update}}^{\#} = 2 \cdot \left(m^2(\gamma + \frac{3}{2}\kappa) + 1 \right) \cdot n \quad (7)$$

The final equations to complete the specification of the rgcLSTM are given below.

$$c^{(t)} = f^{(t)} \odot c^{(t-1)} + f^{(t)} \odot g^{(t)} \quad (8)$$

$$h^{(t)} = f^{(t)} \odot \tanh(c^{(t)}) \quad (9)$$

The \odot symbol denotes elementwise multiplication. κ is constrained to equal n so that the dimensions match for the elementwise multiplication operations. Eqn. 8 uses a “+” operator on the righthand side and this implements the CEC.

Table 1 compares features between our proposed rgcLSTM versus the cLSTM and convLSTM designs. Also, model M18 in Table 20 of the appendix is an alias for rgcLSTM and gives the summary equations for our rgcLSTM model. Similarly, models M1 and M8 are aliases for the cLSTM and convLSTM, respectively, and their summary equations are described in Table 19 of the appendix.

4 | OVERALL ARCHITECTURE

We use our rgcLSTM module within the PredNet predictive coding framework of Lotter et al.⁴, so have named our variant Pred-rgcLSTM²³. The bottom layer of the architecture appears in Figure 3. Our contribution lies in the redesign of the R module where

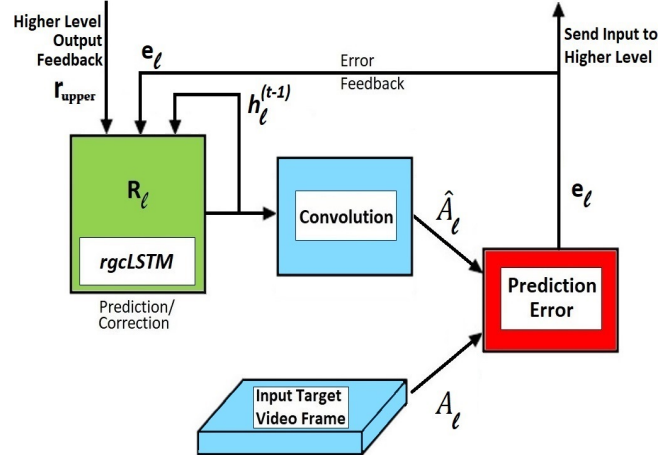


FIGURE 3 The lowest layer of the PredNet architecture with our rgcLSTM module substituted for the cLSTM used in the original PredNet⁴. The layer subscript l is used to signify that higher layers obey the same design, with the caveat that the input to higher layers is prediction error from the immediately lower layer.

our rgcLSTM replaces the cLSTM used by Lotter et al. In this design, whether PredNet or Pred-rgcLSTM, learning primarily occurs within the gated recurrent cells but is triggered by prediction error signals that are input to the R module.

Although Figure 3 shows the lowest layer (because the input is a video frame), we still include layer index subscripts, l , because the higher layers have the same structure (see Figure 4) although the channel counts and image dimensions differ for each layer. The prediction error module drives the gated-recurrent learning (via backpropagation by combining the prediction errors into a cost function). The module calculates the error between the input frame A_l and the predicted output frame \hat{A}_l . The convolution module converts the output of the rgcLSTM, $h_l^{(t)}$, to $\hat{A}_l^{(t)}$ so the dimensions are compatible with A_l for pixelwise subtraction.

The prediction error module stacks the pixelwise difference (Eqn. 12) between the predicted image frame \hat{A}_l and the actual frame A_l by subtracting the two frames and applying the *ReLU* as follows:

$$err1 = \text{ReLU}(\hat{A}_l - A_l) \quad (10)$$

$$err2 = \text{ReLU}(A_l - \hat{A}_l) \quad (11)$$

$$e_l = [err1, err2] \quad (12)$$

In the case of gray scale, e_l is a stack of the two error images encoding negative and positive prediction errors according to Eqns. 10 and 11. The e_l feedback is sent to the rgcLSTM, R_l , and to the next higher layer R_{l+1} after applying downsampling to obtain image dimensions that match the next layer dimensions (see Fig 4). Inputs to the rgcLSTM module are its internal recurrent input and its error feedback. In the multi-layer case, the input contains an additional parameter which is the feedback from the directly higher rgcLSTM block, r_{upper} . These inputs are stacked to fit into the rgcLSTM block.

The rgcLSTM block learns the spatiotemporal changes using the training input data to predict future frames. The update process is a function of the sequential input within one layer of the proposed model as shown in Figure 5. Figure 5 shows three unrollment (unfolding in time) steps and tracks the model from the leftmost (earliest) part of the diagram. In the beginning, the error module evaluates the prediction error by the difference between the assumed default prediction and the first input which is the first video frame. This prediction error then goes to the rgcLSTM module as an input. The rgcLSTM module processes this input, its initial state, and initial output through its internal gates to produce the next predicted video frame as its output. Next, the current output of the rgcLSTM module passes through the error module to evaluate the next prediction error which is forwarded to the next unfolded rgcLSTM module. At this time the prediction error acts as a correction factor for the rgcLSTM module which guides the rgcLSTM module to adjust its weights and state according to the current frame and the previous prediction of this frame. The process repeats until the final predicted frame is processed.

Since our model targets spatiotemporal prediction, we used *hardSig* as the recurrent activation function and *tanh* as the output activation function. *hardSig* was calculated as:

$$\text{hardSig}(x) = \max(\min(0.25x + 0.5, 1), 0). \quad (13)$$

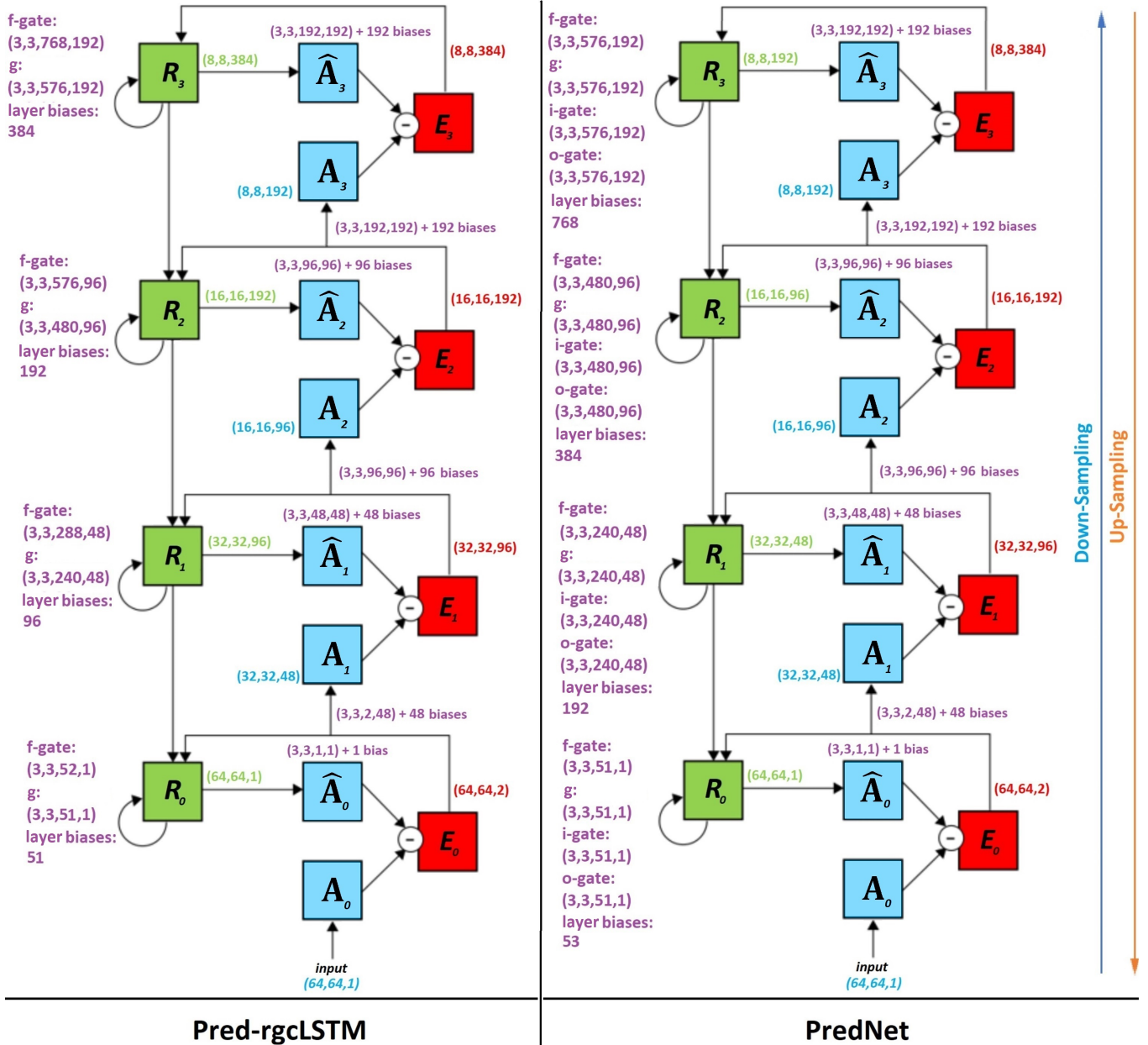


FIGURE 4 The weight counts of each component of both Pred-rgcLSTM and PredNet are based on reference⁴. The input (Moving MNIST) is a 64×64 gray scale image with one channel. A tuple for a gate in the R module of the form (x, x, y, z) signifies a count of z convolution kernels with dimension $x \times x$, each with y input channels.

We chose the *hardSig* because it has shown better empirical results in our earlier experiments than the sigmoid in LSTM spatiotemporal prediction models^{24,25}. The hard saturation may help it escape from local minima²².

We now explain the full multi-layer model shown in Figure 4. Table 2 lists and defines the terms used in the model. The input dimensions of each layer of the four-layered Pred-rgcLSTM and PredNet models are shown in Table 3. h_l is the recurrent output of the rgcLSTM or cLSTM, e_l is the error feedback, c_l is the memory cell of the gated unit (equivalent to $c_{(l-1)}$), and $r_{\text{upper}(l)}$ is the higher-level feedback from layer $l + 1$. R_l is the total dimension of each the forget gate $f^{(l)}$ input stack and Ra_0 is the total dimension of the input stack to the activation unit $g^{(l)}$. Table 4 and Figure 4 show the dimensions of the weights and biases in each layer of rgcLSTM-PredNet as compared to the original PredNet. This is shown for each layer index $l \in \{0, 1, 2, 3\}$. f_l , i_l , o_l are the forget, input and output gates, respectively. g_l is the activation unit. *downsample_l* is the transition kernel from the lower layer to the higher layer. \hat{A}_l is the convolution kernel applied to the rgcLSTM output or the cLSTM output. *Biases* are the total

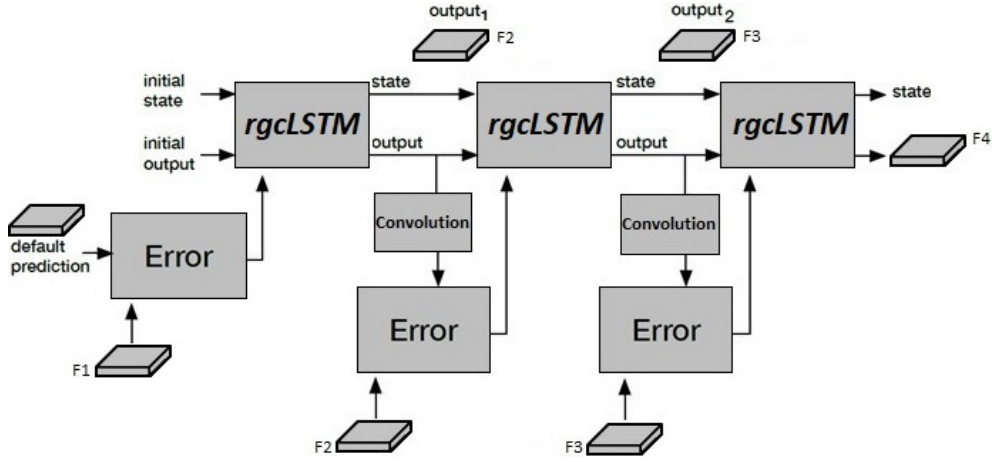


FIGURE 5 Three unrollment steps for the lowest layer of Pred-rgcLSTM using three input frames: F1, F2, and F3. F4 is the next-frame prediction.

TABLE 2 Definition of terms.

Symbol	Meaning
h_l	Eqn. 9.
e_l	Eqn. 12. $e_0 = x$.
c_l	Eqn. 8.
$r_{\text{upper}(l)}$	feedback to R_l from layer $l + 1$.
R_l	dimension of gate input stack ($\gamma + 2\kappa$).
Ra_l	dimension activation input stack ($\gamma + \kappa$).
f_l	Eqn. 4.
g_l	Eqn. 5.
i_l	PredNet input gate for layer l .
o_l	PredNet output gate for layer l .
A_l	next frame input for layer l .
\hat{A}_l	predicted next frame input for layer l .
downsample_l	convolutional downsampling from layer l to $l + 1$.
biases_l	total number of biases in layer l .

number of biases in each layer (i.e., including the gate, activation, downsampling, and the transition between the output of the rgcLSTM and the error module).

In Table 3, Table 4, and Figure 4 we assume that the model input is a gray-scale image of size 64×64 pixels and has a one input channel depth. For the purpose of counting the trainable parameters, the values of m , γ , κ , and n from Section 3 are given in Table 5 for all four layers in the model.

TABLE 3 Dimensions of input components to Pred-rgcLSTM and PredNet for Moving MNIST. A tuple of the form (x, x, y) signifies an $x \times x$ kernel with y input channels. Both models have four layers and the lowest is indexed by the subscript zero.

Parameter	Dimensions	
	Pred-rgcLSTM	PredNet
h_0	(64, 64, 1)	(64, 64, 1)
e_0	(64, 64, 2)	(64, 64, 2)
c_0	(64, 64, 1)	N/A
$r_{\text{upper}(0)}$	(64, 64, 48)	(64, 64, 48)
R_0 gate input stack	(64, 64, 52)	(64, 64, 51)
Ra_0 activation input stack	(64, 64, 51)	(64, 64, 51)
h_1	(32, 32, 48)	(32, 32, 48)
e_1	(32, 32, 96)	(32, 32, 96)
c_1	(32, 32, 48)	N/A
$r_{\text{upper}(1)}$	(32, 32, 96)	(64, 64, 96)
R_1 input stack	(32, 32, 288)	(32, 32, 240)
Ra_1 activation input stack	(32, 32, 240)	(32, 32, 240)
h_2	(16, 16, 96)	(16, 16, 96)
e_2	(16, 16, 192)	(16, 16, 192)
c_2	(16, 16, 96)	N/A
$r_{\text{upper}(2)}$	(16, 16, 192)	(16, 16, 192)
R_2 input stack	(16, 16, 576)	(16, 16, 480)
Ra_2 activation input stack	(16, 16, 480)	(16, 16, 480)
h_3	(8, 8, 192)	(8, 8, 192)
e_3	(8, 8, 384)	(8, 8, 384)
c_3	(8, 8, 192)	N/A
R_3 input stack	(8, 8, 768)	(8, 8, 576)
Ra_3 activation input stack	(8, 8, 576)	(8, 8, 576)

4.1 | Keeping the Gate Output within a Functional Operating Range

From Figure 1 we see that if the module gate value drops to zero, the rgcLSTM cell does an extreme reset: the memory state is forgotten, the current input is ignored, and the output is zero. Within the predictive coding architecture, there are several factors that help keep the gate value within a functional range to avoid this. First, the input image pixel values are normalized to the range $[0, 1]$ and these become the target values for E_0 in the lowest layer of the network (Eqns. 10 and 11). The values for \hat{A}_l are also kept in the range $[0, 1]$. The ReLU serves as a rectifier to keep the e_l within the range $[0, 1]$. These form the inputs $x = e_l$ to the rgcLSTM. Within the rgcLSTM, the values of h and c (Figure 1) are constrained to fall in the range $(-1, 1)$ because they are outputs of a tanh or a gate modulated tanh. Finally, the module gate uses a hard sigmoid configured to be linear in the range $[-2, 2]$. The inputs to the hard sigmoid stay well within this range, thereby keeping the gate functional.

5 | METHODS

Experiments were performed to compare our rgcLSTM used in Pred-rgcLSTM with the standard cLSTM used in PredNet. We show that our rgcLSTM achieves the same or better accuracy than the standard cLSTM using a smaller parameter budget, less training time, and smaller memory requirements. To build Pred-rgcLSTM, we modified the code for PredNet which is available at <https://github.com/coxlab/prednet>. In all of our simulations and experiments, the gate activation for the rgcLSTM cells was hardsig set to be linear over the range $[-2, 2]$. To make the timing results comparable for both models, the only

TABLE 4 Dimensions of kernel (weight) components of Pred-rgcLSTM and PredNet for Moving MNIST.

Kernel	Dimensions	
	Pred-rgcLSTM	PredNet
f_0	(3, 3, 52, 1)	(3, 3, 51, 1)
g_0	(3, 3, 51, 1)	(3, 3, 51, 1)
i_0	N/A	(3, 3, 51, 1)
o_0	N/A	(3, 3, 51, 1)
\hat{A}_0	(3, 3, 1, 1)	(3, 3, 1, 1)
$downsample_0$	(3, 3, 2, 48)	(3, 3, 2, 48)
$biases_0$	51	53
f_1	(3, 3, 288, 48)	(3, 3, 240, 48)
g_1	(3, 3, 240, 48)	(3, 3, 240, 48)
i_1	N/A	(3, 3, 240, 48)
o_1	N/A	(3, 3, 240, 48)
\hat{A}_1	(3, 3, 48, 48)	(3, 3, 48, 48)
$downsample_1$	(3, 3, 96, 96)	(3, 3, 96, 96)
$biases_1$	240	336
f_2	(3, 3, 576, 96)	(3, 3, 480, 96)
g_2	(3, 3, 480, 96)	(3, 3, 480, 96)
i_2	N/A	(3, 3, 480, 96)
o_2	N/A	(3, 3, 480, 96)
\hat{A}_2	(3, 3, 96, 96)	(3, 3, 96, 96)
$downsample_2$	(3, 3, 192, 192)	(3, 3, 192, 192)
$biases_2$	480	672
f_3	(3, 3, 768, 192)	(3, 3, 576, 192)
g_3	(3, 3, 576, 192)	(3, 3, 576, 192)
i_3	N/A	(3, 3, 576, 192)
o_3	N/A	(3, 3, 576, 192)
\hat{A}_3	(3, 3, 192, 192)	(3, 3, 192, 192)
$biases_3$	576	960
Total training params	4,316,235	6,909,834

TABLE 5 Dimension parameters for the gated module (either rgcLSTM or cLSTM) for each of the four layers for the moving MNIST dataset.

Parameter	Layer ₀	Layer ₁	Layer ₂	Layer ₃
m	3	3	3	3
γ	50	192	384	384
κ	1	96	192	384
n	1	96	192	384

modification to the code was to replace the cLSTM with the rgcLSTM of compatible size to ensure the comparisons were fair. Our rgcLSTM source code is available at the following link <https://github.com/NellyElsayed/rgcLSTM>.

Two experiments were conducted on next-frame(s) prediction of a spatiotemporal (video) sequence: one for a gray-scale dataset (moving MNIST) and the other for an RGB dataset (KITTI traffic). A third experiment is described later. The moving MNIST dataset¹² is a good example of how the model can determine movement of two specific objects within a frame and how the model can handle new object shapes and movement directions. The KITTI dataset²⁶ requires the model to track several

TABLE 6 Experimental conditions in the Moving MNIST experiment for recurrent gate-based blocks. These correspond to experiments shown in Table 7. N/A means there cannot be peephole connections because there is no memory cell state.

Model	Memory Cell	Gates	Peephole
rgcLSTM	Yes	1	Yes
LSTM	Yes	3	No
PLSTM	Yes	3	Yes
GRU	No	2	N/A
MGU	No	1	N/A

different moving and non-moving objects within a frame The roof-mounted camera records vehicle traffic which has both static objects (scene) and dynamic objects (moving vehicles). Also, it shows how the model can deal with 3-channel RGB videos. For both experiments, we trained our model using four layers like that shown in Figure 3. The number of parameters and inputs are the same except for the first layer in each experiment, due to the input different input sizes for moving MNIST versus KITTI. The loss function was a weighted combination of the mean-squared-error output by the modules $E_0 \dots E_3$. Lotter et al.⁴ found that the best weighting was $[1, 0, 0, 0]$, so our experiments used that choice. Both experiments used the Adam optimizer²⁷ with an initial learning rate $\alpha = 0.001$ and a decay factor of 10 after half of the training process, and $\beta_1 = 0.9$ and $\beta_2 = 0.999$. Frame size was downsampled by factor of 2 moving upwards through the layers and upsampled by factor of 2 moving down the layers.

For training elapsed time comparisons in Experiment 1, the model was trained on an Intel(R) Core i7-7820HK CPU with 32GB memory and an NVIDIA GeForce GTX 1080 graphics card. For Experiment 2, both Pred-rgcLSTM and PredNet were trained on Intel(R) Core i7-6700 @4.00GHz8 processor with 64 GB memory and NVIDIA GeForce GTX 980 Ti/PCIe/SSE2 graphics card.

The methods for Experiment 3 are different than Experiments 1 and 2, so they are described later in Section 5.3.1.

5.1 | Experiment 1: The Moving MNIST Dataset

Although the original PredNet model was not tested on the Moving MNIST dataset, we considered it appropriate to start with this simpler dataset for our experiments. This experiment compared the video prediction performance of our rgcLSTM-PredNet with the original PredNet.

5.1.1 | Method

The Moving MNIST dataset consists of 10,000 video sequences of two randomly selected moving digits sampled from the original MNIST dataset. Each sequence is 20 frames long, with a frame size of 64x64 grayscale pixels. Thus, each frame has a depth of one channel. We divided the dataset into 6,000 video sequences for training, 3,000 for validation and 2,000 for testing. The training process was completed in one epoch. The number of core-channels in each layer were 1, 48, 96, and 192 respectively. Hence, the dimensions of weights and inputs are shown in Tables 3 and 4, and Figure 4.

Our simulations are performed using rgcLSTM-PredNet and PredNet but, in the results section, we compare our simulation results with several spatiotemporal prediction approaches that use recurrent gated units. Table 6 shows the properties of the models we consider. These properties are the existence of a memory cell, the number of gates, and the existence of peephole connections. The models we compare are our novel rgcLSTM, the standard LSTM¹⁹, the peephole LSTM (PLSTM)²⁸, the gated recurrent unit (GRU)¹⁶, and the minimal gated unit (MGU)¹⁷.

5.1.2 | Results of Experiment 1

Table 7 shows performance comparisons among several models for moving MNIST. We compared Pred-rgcLSTM with several other unsupervised recurrent gate-based models (i.e., either LSTM or GRU based models) for the moving MNIST dataset.

TABLE 7 Moving MNIST performance comparison.

Model	Type	MSE	MAE	SSIM
FCLSTM ^{8,12}	LSTM	1.865	2.094	0.690
CDNA ^{29,13}	cLSTM	0.974	1.753	0.721
DFN ^{29,30}	DynamicFilters	0.890	1.728	0.726
VPN ^{29,31}	cLSTM	0.641	1.310	0.870
ConvLSTM ^{29,8}	convLSTM	1.420	1.829	0.707
ConvGRU ^{29,32}	convGRU	1.254	2.254	0.601
TrajGRU ^{29,32}	convGRU	1.138	1.901	0.713
PredRNN++ ²⁹	convLSTM	0.465	1.068	0.898
PredRNN ^{33,29}	convLSTM	0.568	1.261	0.867
PredNet ⁴	cLSTM	0.011	0.049	0.915
Pred-rgcLSTM	rgcLSTM	0.009	0.017	0.924

TABLE 8 Moving MNIST average elapsed training time and standard error (n=15).

Model	Training Time (m)	Standard Error (SE)
PredNet	100.328	0.586532
Pred-rgcLSTM	73.561	0.297411

TABLE 9 Moving MNIST memory required to save Pred-rgcLSTM and PredNet trained parameters.

Model	Memory
PredNet	81.068 MB
Pred-rgcLSTM	50.650 MB

Performance measures included mean squared error (MSE), mean absolute error (MAE), and the structural similarity index (SSIM)³⁴ which is a measure for image quality similarity structure between predicted and actual images. We also compared our model to PredNet. For the remaining models that we were unable to test due to hardware limitations we obtained the results from their published work. All of the models are convolutional variants. Our Pred-rgcLSTM shows a reduction of both the MSE and MAE compared to all of the other models tested. This includes FCLSTM¹², CDNA¹³, DFN³⁰, VPN³¹, ConvLSTM⁸, ConvGRU, TrajGRU³², PredRNN³³, PredRNN++²⁹ and PredNet⁴. The main comparison is between our rgcLSTM block and the cLSTM block using the same model architecture. Our model also has the best structural similarity index measurement (SSIM) among the tested models.

The training time in minutes for the Pred-rgcLSTM and PredNet models for one batch of 6,000 trials is shown in Table 8. Replacing the rgcLSTM cell with the cLSTM reduced elapsed training time by about 26% for training moving MNIST for one epoch. Table 8 also shows the SE of model training time for both the cLSTM and our rgcLSTM model. The sample size was $n = 15$ for each model.

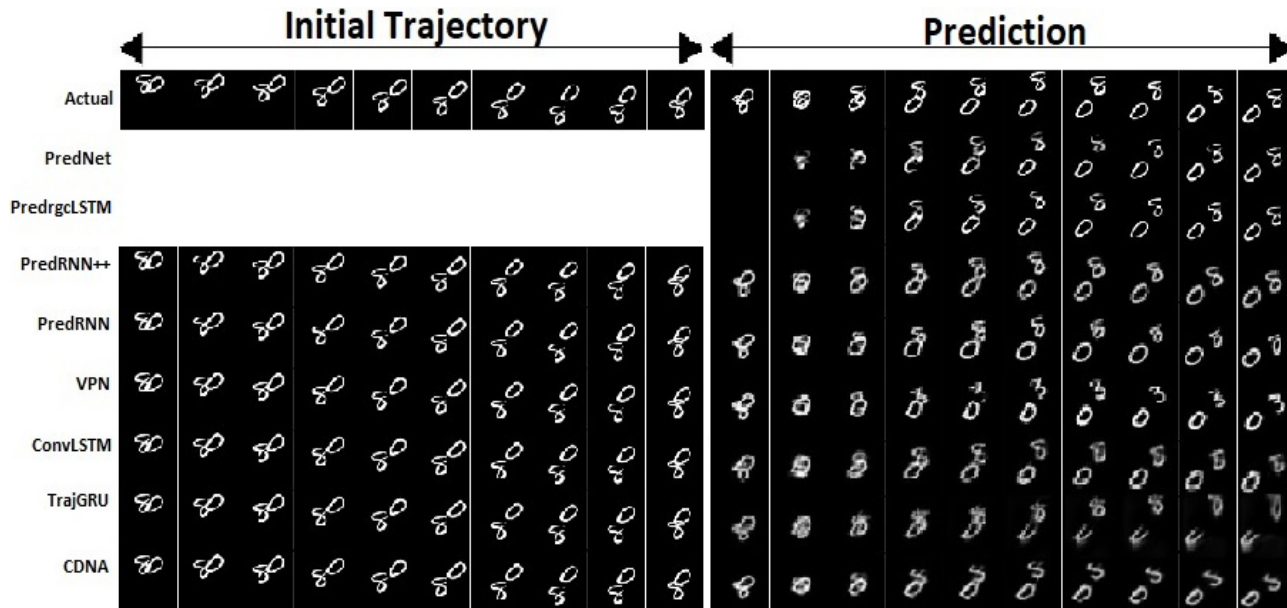
For the cLSTM, the number of parameters is calculated by:

$$\begin{aligned} \text{cLSTM}_{\text{cell}}^{\#} &= f_{\text{gate}}^{\#} + g_{\text{update}}^{\#} + i_{\text{gate}}^{\#} + o_{\text{update}}^{\#} \\ &= 4 \cdot ((m^2(\gamma + \kappa) + 1) \cdot n) \end{aligned} \quad (14)$$

Here, $i_{\text{gate}}^{\#}$ and $o_{\text{gate}}^{\#}$ are the number of trainable parameters for the input and output gates of the standard convLSTM cell. The multiplication by four is due to the input update activation, forget gate, input gate, and output gate that each has the same number

TABLE 10 Moving MNIST: the number of trainable parameters in each model.

Model	Trainable Parameters
PredNet	6,909,834
ConvGRU	8,010,000
TrajGRU	4,770,000
ConvLSTM	7,585,296
FCLSTM	142,667,776
Pred-rgcLSTM	4,316,235

**FIGURE 6** Visual results of Moving MNIST predictions after training based on our rgcLSTM and other models.

of trainable parameters. Each cLSTM gate uses the same number of parameters as the g_{update} gate in the rgcLSTM. Recall that Eqn. 7 gives the parameter count for our rgcLSTM. By comparing Eqns. 7 and 14, we see that the number of trainable parameters is reduced approximately by 40% in the rgcLSTM compared to the cLSTM.

We also compared the memory needed (MB) to save the Pred-rgcLSTM and PredNet trained models. This is shown in Table 9. The training parameters of the Pred-rgcLSTM and the PredNet were saved using the Keras API and the size of each file was examined. Pred-rgcLSTM required significantly less memory than PredNet.

Using the Keras API `model.count_params()`⁵, we compared the number of training parameters used in Pred-rgcLSTM and PredNet of the implemented models in Table 10. For the remaining models in Table 10, we obtained the results from their published work^{32,8,12} which also were counted by using the same Keras API method⁵. The empirical parameter counts for the implemented PredNet and Pred-rgcModels match the counts given in the design specifications shown in Table 4, giving some measure of confidence that these two models are implemented correctly. Our model uses the fewest parameters of the tested models. Our model has fewer trainable parameters approximately by 40%-50% than the ConvGRU and ConvLSTM respectively. Our Pred-rgcLSTM model that is based on rgcLSTM block has approximately 40% fewer trainable parameters than the original PredNet model that uses cLSTM modules. This latter claim can be confirmed by examining the calculations in Table 4.

For Experiment 1, an example prediction for the moving MNIST dataset is shown in Figure 6 for nine different models. In contrast to most of the models, neither PredNet nor our Pred-rgcLSTM require an initial input trajectory for predicting the upcoming frames. They use only the current frame and current state of the trained LSTM to predict the next frame. Our rgcLSTM

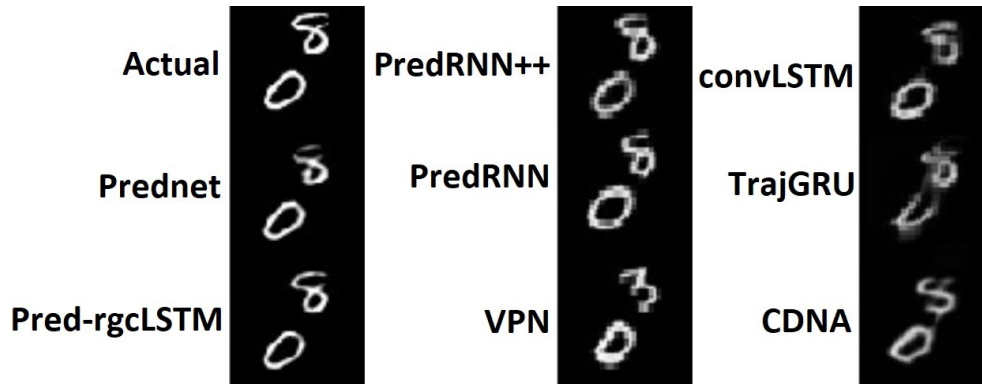


FIGURE 7 Magnified visual result of Moving MNIST predictions for prediction time step 6 after training based on our rgcLSTM and other models.

TABLE 11 KITTI dataset experiment dimensions of kernel (weight) components of the first layer of Pred-rgcLSTM and PredNet.

Kernel	Pred-rgcLSTM	PredNet
f_0	(3, 3, 60, 3)	(3, 3, 57, 3)
g_0	(3, 3, 57, 3)	(3, 3, 57, 3)
i_0	N/A	(3, 3, 57, 3)
o_0	N/A	(3, 3, 57, 3)
\hat{A}_0	(3, 3, 3, 3)	(3, 3, 3, 3)
$downsample_0$	(3, 3, 6, 48)	(3, 3, 6, 48)
$biases_0$	60	57

demonstrates comparable results with the other models and finds better visual contours than the cLSTM used in PredNet. To see the improved prediction in better detail, Figure 7 magnifies the predicted images (taken from Figure 6) for prediction time step six for each model.

5.1.3 | Discussion of Experiment 1

This experiment shows that the version of PredNet which uses our novel rgcLSTM modules gives state-of-the-art video prediction performance in comparison to a range of models, as seen in Table 7. In particular, its performance is on par with the original PredNet, which uses the cLSTM instead of our rgcLSTM.

Furthermore, our rgcLSTM version of PredNet is significantly more cost effective than the original PredNet. Specifically, the parameter count is reduced by about 40%, the memory needed to save the trained parameters is reduced by about 38%, and the elapsed training time is reduced by about 27%.

5.2 | Experiment 2: KITTI Dataset

Experiment 2 was conducted to compare the rgcLSTM-PredNet performance with the original PredNet on another dataset besides Moving MNIST. The KITTI traffic dataset was chosen because it was used in the original PredNet experiments. Its dimensions were resized as described at: <http://github.com/coxlab/prednet>.

TABLE 12 KITTI dataset experiment dimensions of input component of Pred-rgcLSTM and PredNet. The N/A entries indicate that PredNet does not have peephole connections.

Parameter	Pred-rgcLSTM	PredNet
h_0	(128, 160, 3)	(128, 160, 3)
e_0	(128, 160, 6)	(128, 160, 6)
c_0	(128, 160, 3)	N/A
$r_{upper(0)}$	(128, 160, 48)	(128, 160, 48)
R_0 gate input stack	(128, 160, 60)	(128, 160, 57)
Ra_0 activation input stack	(128, 160, 57)	(128, 160, 57)
h_1	(64, 80, 48)	(64, 80, 48)
e_1	(64, 80, 96)	(64, 80, 96)
c_1	(64, 80, 48)	N/A
$r_{upper(1)}$	(64, 80, 96)	(64, 80, 96)
R_1 input stack	(64, 80, 288)	(64, 80, 240)
Ra_1 activation input stack	(64, 80, 240)	(64, 80, 240)
h_2	(32, 40, 96)	(32, 40, 96)
e_2	(32, 40, 192)	(32, 40, 192)
c_2	(32, 40, 96)	N/A
$r_{upper(2)}$	(32, 40, 192)	(32, 40, 192)
R_2 input stack	(32, 40, 576)	(32, 40, 480)
Ra_2 activation input stack	(32, 40, 480)	(32, 40, 480)
h_3	(16, 20, 192)	(16, 20, 192)
e_3	(16, 20, 384)	(16, 20, 384)
c_3	(16, 20, 192)	N/A
R_3 input stack	(16, 20, 768)	(16, 20, 576)
Ra_3 activation input stack	(16, 20, 576)	(16, 20, 576)

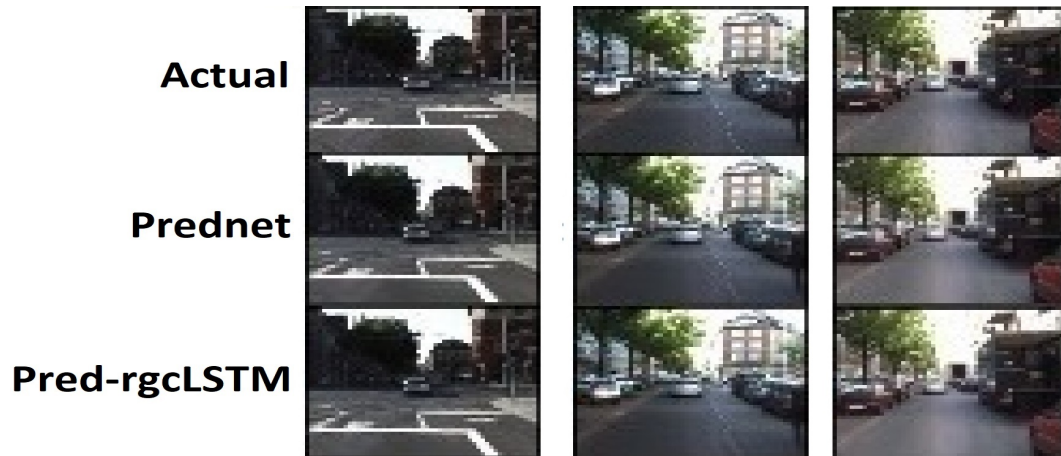
5.2.1 | Method

The experimental method is essentially the same as was used for the Moving MNIST dataset as described at the beginning of Section 5. Any differences in method stem from modifying the architecture to accommodate the larger input dimensions of the KITTI dataset. The KITTI dataset²⁶ is a collection of real life traffic videos captured by a roof-mounted camera on a car driving in an urban environment. The data is divided into three categories: city, residential, and road. Each category contains 61 different recorded sessions (i.e., different video sequences) which were divided into 57 sessions for training and four for validation. Simulations were performed for both our rgcLSTM-PredNet and the original cLSTM-PredNet. For training, both models used the same initialization, training, validation, and data down-sampling which was used by Lotter et al.⁴. Each input image frame size was 128×160 pixels, where the image height is 128 pixels and the image width is 160, and three RGB channels. The total length of the training dataset (of the 57 sessions) was approximately 41K frames. The model was trained for 150 epochs.

The architecture is very similar to that used in Experiment 1. The number of kernels (output channels) in each R layer, indicated by the value of the last component of h_i in Table 12, were 3, 48, 96, and 192, respectively. The resulting dimension changes for the weights in layer R_0 are shown in Table 11. The other layer weight dimensions are unchanged from Table 4. The input dimensions for each layer are changed in layer R_0 (because of the increased image channels and dimensions as compared to Moving MNIST) in the width and height and number of input channels of the original video frame. However, the higher layers have changes only in the width and height dimensions.

TABLE 13 Performance comparison on the KITTI traffic video dataset.

Model	Train Time	# Params	MSE	MAE	SSIM	Memory
PredNet	230.982405	6,915,948	0.0044	0.0347	0.911	81.142 MB
Pred-rgcLSTM	140.530364	4,320,273	0.0035	0.030	0.932	50.697 MB

**FIGURE 8** Next-frame prediction on the KITTI dataset. The predicted image is used as input for predicting the next frame.**FIGURE 9** The magnified visual results for the KITTI dataset prediction for the 6th prediction step for Pred-rgcLSTM and PredNet.

5.2.2 | Results of Experiment 2

Table 13 shows the results for the KITTI dataset benchmark including elapsed training time (minutes), number of trainable parameters, mean squared error (MSE), mean absolute error (MAE), and mean structural similarity index measurement (SSIM)³⁴ of our rgcLSTM and cLSTM. The sample size is $n = 16$ for each of these measures. The rgcLSTM has a higher SSIM than the cLSTM. Table 13 also shows the memory needed (MB) to save the trainable model for both Pred-rgcLSTM and PredNet. The rgcLSTM uses fewer trainable parameters. Also, the training time is reduced by about 40% – 50% as in the moving MNIST (gray-scale) prediction task and a smaller SE, MSE, and MAE values.

For the KITTI dataset, sample visual testing results comparing our rgcLSTM and the cLSTM appear in Figure 8. This figure shows that the rgcLSTM (with smaller training time and parameter count) matches the accuracy in comparison to the cLSTM. To compare the accuracy more clearly between the rgcLSTM and cLSTM, images of prediction step 6 are magnified for each model. This is shown in Figure 9. The predictions for both models in comparison to ground truth are perceptually indistinguishable (although the images have limited resolution).

Figure 10 shows the training and validation loss through 150 epochs of the KITTI dataset training using both the proposed Pred-rgcLSTM and PredNet. The graphs show that the training and validation losses of both models is nearly identical suggesting

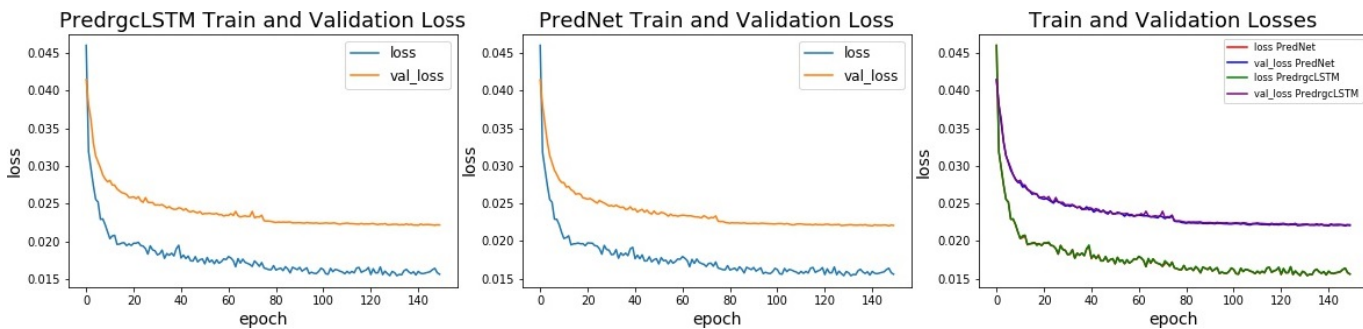


FIGURE 10 Example KITTI dataset training and validation losses for both Pred-rgcLSTM and PredNet. Left: Pred-rgcLSTM. Middle: PredNet. Right: both graphs are superimposed.

that both models may be approaching the limit in Bayesian prediction error. The details of the random walk match closely in both models. This phenomenon is robust as we have observed it in other simulation runs. It suggests the rgcLSTM captures the nature of the cLSTM computation in great detail.

5.2.3 | Discussion of Experiment 2

The general pattern of results found in Experiment 1 using the Moving MNIST dataset was reproduced in our second experiment that used the KITTI dataset. First, performance was nearly equivalent for both models. Second, the cost-effectiveness of rgcLSTM-PredNet in relation to PredNet persists. In particular, the parameter count, memory needed to store the trained weights, and the training time are all greatly reduced.

5.3 | Experiment 3: Studying the Space of Reduced Models

The good performance of the rgcLSTM version of PredNet raises the following question. The three gates of the standard LSTM must serve some purpose. It seems too good to be true that the one gate of the rgcLSTM could effectively learn to perform the three different gate functions of a standard LSTM, and thereby act as a multi-function gate. It suggests that the separate gates of the standard LSTM have excess learning capacity for the Moving MNIST and KITTI prediction tasks and that the single set of shared weights of a single gate can learn to perform all three different functions. To explore this possibility further, we enumerated a subspace of gated recurrent architectures and examined their performance on both the Moving MNIST and KITTI datasets.

5.3.1 | Method

We studied two sets of gated networks that included a total of twenty models. The first was a set of fourteen *single-function* gate models. The second set consisted of six *multi-function* gate models.

First, we explain how the single-function gate models were chosen. We started with the full three-gate convLSTM of Shi et al.⁸ which included elementwise peephole connections. In addition to the peephole connections, this architecture has three gates. We include it in the set. Next, we obtain three two-gate architectures by removing one of the three gates from the original convLSTM. Finally, there are three ways to include one gate. This yields a total of $1+3+3=7$ architectures. For each of these architectures, we can choose to use an elementwise peephole connection, or not. The elementwise version is used because we are considering reductions of the Shi et al.⁸ model. This gives $2 \cdot 7 = 14$ architectures.

Next, we explain how the multi-function gate models were chosen. The goal here is to create reduced models of our rgcLSTM. Like our rgcLSTM, each of these models has exactly one gate. Because it is a multi-function gate, this gate is constrained to perform more than one function simultaneously. In all cases, the gate serves as a forget gate. The gate can also be used to perform either one or two other functions, yielding three cases:

1. The gate serves all three functions.
2. The gate serves two functions, specifically a forget gate and also as an input gate.

TABLE 14 The single-function gate performance for the oving MNIST datas set.

Model	Peephole	f-gate	i-gate	o-gate	MSE	MAE	SSIM	Memory(MB)	# parameters
M1	No	✓	✓	✓	0.010	0.019	0.915	81.068	6,909,834
M2	No	✓	-	-	0.043	0.050	0.623	44.479	3,880,786
M3	No	✓	✓	-	0.043	0.050	0.623	61.822	5,395,310
M4	No	✓	-	✓	0.012	0.022	0.890	61.825	5,395,310
M5	No	-	✓	-	0.043	0.050	0.623	44.479	3,880,786
M6	No	-	✓	✓	0.043	0.050	0.623	61.822	5,395,310
M7	No	-	-	✓	0.043	0.050	0.623	44.479	3,880,786
M8	Yes	✓	✓	✓	0.010	0.019	0.914	94.121	8,216,229
M9	Yes	✓	-	-	0.043	0.050	0.623	49.461	4,316,251
M10	Yes	✓	✓	-	0.013	0.023	0.881	71.790	6,266,240
M11	Yes	✓	-	✓	0.043	0.050	0.623	71.791	6,266,240
M12	Yes	-	✓	-	0.043	0.050	0.623	49.463	4,316,251
M13	Yes	-	✓	✓	0.043	0.050	0.623	71.791	6,266,240
M14	Yes	-	-	✓	0.020	0.032	0.813	49.463	4,316,251

TABLE 15 The multi-function gate performance for the Moving MNIST dataset.

Model	Peephole	Acting Gate	Shared Effect	MSE	MAE	SSIM	Memory(MB)	# parameters
M15	No	f-gate	i-gate, o-gate	0.009	0.018	0.918	44.479	3,880,786
M16	No	f-gate	i-gate	0.043	0.050	0.623	44.479	3,880,786
M17	No	f-gate	o-gate	0.011	0.020	0.908	44.479	3,880,786
M18	Yes	f-gate	i-gate, o-gate	0.009	0.017	0.925	50.650	4,316,235
M19	Yes	f-gate	i-gate	0.013	0.024	0.879	50.650	4,316,235
M20	Yes	f-gate	o-gate	0.015	0.025	0.860	50.650	4,316,235

3. The gate serves two functions, specifically a forget gate and also as an output gate.

Finally, we can make the choice to add, or not add, a (convolutional) peephole connection. The convolutional peephole connection was used because we are considering reductions of the rgcLSTM model (which used convolutional peephole connections). This gives $2 \cdot 3 = 6$ architectures.

The twenty resulting architectures are shown in the appendix. The equations for models M1 through M14 are shown in Table 19 and describe the single-function gate architectures. The equations for models M15 through M20 are shown in Table 20 and describe the multi-function gate architectures.

M1 is an alias for the cLSTM architecture used in the original Lotter et al.⁴ model and M8 is an alias for the Shi et al.⁸ convLSTM with elementwise peephole connections. M18 is an alias for our rgcLSTM architecture having a single gate with three functions as well as a convolutional peephole connection.

5.3.2 | Results for the Moving MNIST Data Set

This section reports the results for all twenty models on the Moving MNIST dataset. The following section will report results for the KITTI dataset. Table 14 describes the single-function gate models and shows the mean MSE, MAE, and SSIM. The means are based on fifteen simulation runs. Also shown is the memory consumed by each model and the parameter count. By all three performance measures (MSE, MAE, and SSIM), models M1 (cLSTM) and M8 (convLSTM) gave the best performance. Of these two models, M1 had the lower memory requirement and parameter count.

Table 15 reports the performance for the multi-function gate models. Models M15 and M18, which each use a 3-function gate, perform better than the other models which use a 2-function gate. Recall that M18 is an alias for our rgcLSTM and M15 is a non-peephole version of M18, the np-rgcLSTM.

The single-gate models M2, M5, M7, M9, M12, and M14 from Table 14 can be meaningfully compared with models M16, M17, and M18 in Table 15. These models are also multi-function gate models in the degenerate case where the gate performs only one function. With the exception of M14, their performance is the same as the worst performing 2-function gate model in Table 15. This reflects the trend that when the number of gate functions is reduced from three to two to one, performance is reduced.

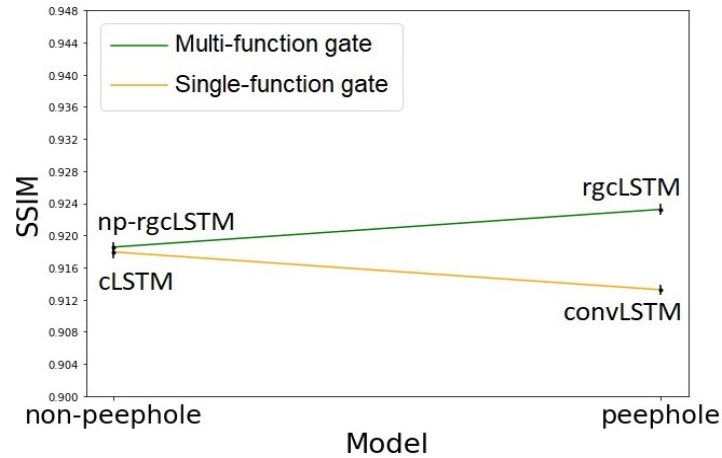


FIGURE 11 The SSIM for the single-function and multi-function gate architectures for the Moving MNIST dataset video prediction.

TABLE 16 Total number of observations, mean SSIM, standard deviation, standard error, and the 95% confidence interval grouped by the models with respect to the SSIM over the moving MNIST prediction.

Model	N	Mean SSIM	SD	SE	95% Conf. Interval
cLSTM	15	0.915	0.00156	0.00040	0.9171-0.9187
convLSTM	15	0.913	0.00124	0.00032	0.9126-0.9139
np-rgcLSTM	15	0.919	0.00134	0.00035	0.9179-0.9190
rgcLSTM	15	0.924	0.00144	0.00037	0.9225-0.9240

TABLE 17 Post-hoc testing over the four models shown in Figure 11 for the Moving MNIST video prediction task.

Group1	Group2	MeanDiff	Lower	Upper	Reject
cLSTM	np-rgcLSTM	0.0006	-0.0007	0.002	False
cLSTM	rgcLSTM	0.0053	0.0039	0.0067	True
cLSTM	convLSTM	-0.0047	-0.0061	-0.0034	True
np-rgcLSTM	rgcLSTM	0.0047	0.0033	0.006	True
np-rgcLSTM	convLSTM	-0.0053	-0.0067	-0.004	True
rgcLSTM	convLSTM	-0.01	-0.0114	-0.0087	True

The SSIM performance of the four winning models (M1, M8, M15, and M18) is plotted in Figure 11. The plot is broken down by presence or absence of a peephole connection and whether the model used single-function or multi-function gates. 95% confidence interval error bars are displayed on the figure and were calculated according to Table 16. A two-way analysis of variance revealed that there was a significant interaction ($p < .05$) between the presence/absence of peephole connections and model type (single-function versus multi-function gate). The figure shows that the peephole connection reduced performance of the cLSTM but improved performance of the rgcLSTM. The post-hoc comparison in Table 17 shows that all comparisons are different except for the cLSTM versus np-rgcLSTM, which is easily seen in Figure 11. We will postpone further discussion until after we report the results for the KITTI dataset.

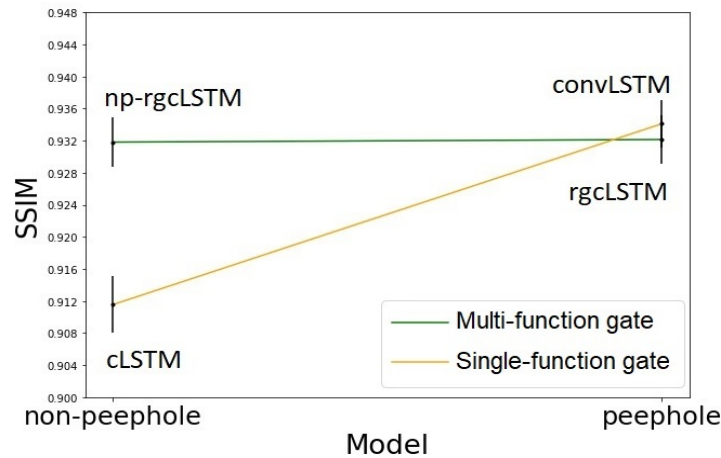


FIGURE 12 The SSIM for the single-function and multi-function gate architectures for the KITTI dataset video prediction.

TABLE 18 Post-hoc testing over the four models shown in Figure 12 for KITTI video prediction task.

Group1	Group2	MeanDiff	Lower	Upper	Reject
cLSTM	np-rgcLSTM	0.0203	0.0119	0.0286	True
cLSTM	rgcLSTM	0.0206	0.0123	0.0289	True
cLSTM	convLSTM	0.0226	0.0142	0.0309	True
np-rgcLSTM	rgcLSTM	0.0003	-0.008	0.0087	False
np-rgcLSTM	convLSTM	0.0023	-0.006	0.0106	False
rgcLSTM	convLSTM	0.002	-0.0064	0.0103	False

5.3.3 | Results for the KITTI Data Set

We selected the four winning Moving MNIST models (M1, M8, M15, M18) for comparative study on the KITTI dataset. Figure 12 shows the SSIM performance results for the four models with 95% confidence intervals. Qualitatively, the pattern of results differs from those shown in Figure 11 for the Moving MNIST dataset. This time the peephole connections improve the performance of the cLSTM but have no effect for the rgcLSTM. A two-way ANOVA reveals that the interaction is significant ($p < .05$). The post-hoc comparisons in Table 18 indicate that the cLSTM performs worse than the other three models on the KITTI dataset.

5.3.4 | Discussion of Experiment 3

This experiment was performed to explore the space of single-function and multi-function gated models in an effort to resolve the question of how our rgcLSTM can successfully use one gate to perform functions that normally use three gates, as in the cLSTM. We found that when these models were substituted into Lotter et al.'s PredNet on the Moving MNIST dataset, the best performing models included our rgcLSTM and Lotter et al.'s cLSTM, according to the MSE, MAE, and SSIM performance measures. When broken down by two factors: 1) whether or not peephole connections were used; and 2) whether single-function or multi-function gates were used, the best performing models for each of these conditions were cLSTM, convLSTM, np-rgcLSTM, and rgcLSTM as shown in Tables 14, 15, and 16. This result is also visualized in Figure 11 and corroborates Experiment 1 where the rgcLSTM performed better than the cLSTM. These results confirm that the rgcLSTM performance makes empirical sense, which was the original motivation for Experiment 3. This is seen in Table 15 and in the performance the single-gate models M2, M5, M7, M9, and M12. For a single gate, as the number of gate functions decreases from three to one, the performance decreases.

When we studied these four models on the KITTI dataset, we still found that the rgcLSTM performed best but also that the performance of the convLSTM of Shi et al.⁸ performed better than the cLSTM used by Lotter et al. This result is specific to the

KITTI dataset and was not found for the Moving MNIST dataset. The other conclusion from this experiment is that the pattern of relative performance of these models varies with dataset.

6 | CONCLUSION

The novelty of our new rgcLSTM architecture lies in the following aspects. First, there is one multi-function gate which serves the function of the forget, input, and output gates. Because only one gate is used, this reduces the number of gate parameters to one third that of the cLSTM or convLSTM. Second, in this reduced parameter, multi-function gate model there is still a peephole connection from the cell memory state to the module gate which allows the cell memory to maintain control over the module gate, in contrast to the cLSTM. Finally, the rgcLSTM uses a convolutional architecture and, because of this, we have replaced the elementwise multiply peephole operation originally used in Shi et al.⁸ with a convolutional peephole connection. Because the peephole connection is convolutional, the associated weight sharing, reduces the parameter count that would be required if an elementwise peephole connection was used. This change deviates from the convLSTM, yet is still compatible with the image processing needs of a convolutional LSTM. Our experiments show that these changes support the model's ability for state-of-the-art video prediction. Thus, the proposed rgcLSTM model reduces the number of trainable parameters, training time, and memory requirements.

The results of Experiments 1 and 2 were consistent with each other and did not reveal any difference in how the rgcLSTM-PredNet model processed the datasets. A more detailed study was performed in Experiment 3 involving a large set of possible reduced parameter, single-function gate architectures and multi-function gate architectures. It was shown that the PredNet variants using the rgcLSTM, cLSTM, and convLSTM modules performed best on the Moving MNIST dataset. This confirms the effectiveness of our rgcLSTM as well as the earlier choice of the cLSTM in the literature. It also confirms that the convLSTM, not used by Lotter et al., would also have been a good choice. Experiment 3 also reveals performance differences between the Moving MNIST and KITTI datasets in regard to choice of architecture. Specifically, the rgcLSTM performed best on the Moving MNIST dataset and peephole connections reduced performance when using single-function gate convolutional LSTMs. On the KITTI dataset, the pattern of results was different. Including peephole connections had no effect when using an rgcLSTM, but yielded a significant improvement when using a convolutional LSTM.

For future work, experiments are needed on a larger sample of datasets to see whether there is some kind of consistent performance pattern across datasets. Experiments are also needed that use more challenging datasets to give the rgcLSTM model a stress test to see when and if its multi-function gates are overwhelmed by a more challenging dataset. Finally, the gated recurrent unit (GRU) model was the first multi-function gate model used in the literature. Future experiments should compare the GRU with the rgcLSTM. Although Experiment 3 studied six different multi-function gate models, it omitted the GRU because it did not fit within our enumeration scheme.

Despite this parameter reduction, the proposed rgcLSTM model performs at a state-of-the-art level on the datasets studied. Because of the reduced parameter count, memory footprint, and training time, our rgcLSTM model is an attractive candidate for future hardware implementation on small and mobile devices.

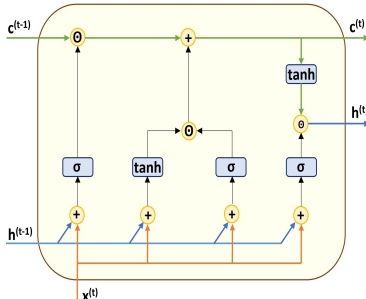
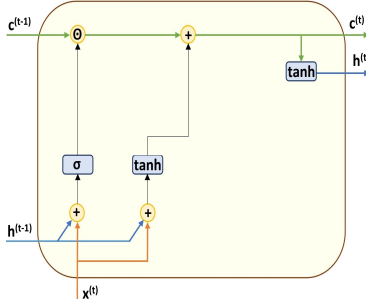
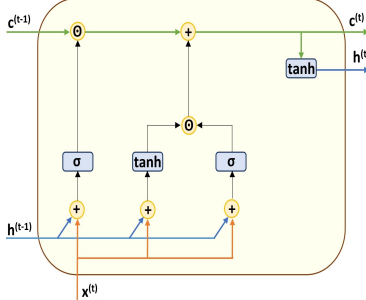
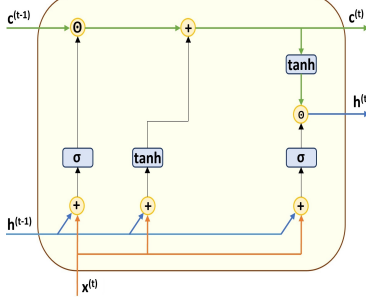
7 | APPENDIX

Tables 19 and 20 show the equations and cell diagrams for the models used in Experiment 3. Table 19 describes the single-function gate models. Table 20 describes the multi-function gate models.

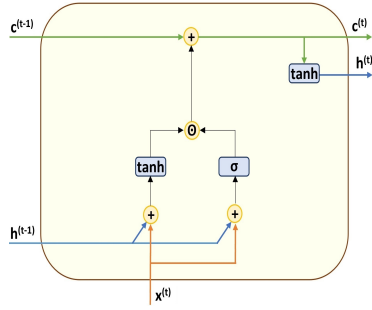
TABLE 19 The fourteen single-function gate convolutional LSTM variants. M1 is an alias for the cLSTM⁴ and M8 is an alias for the convLSTM⁸.

Model **Diagram**

Formulas

M1		$f^{(t)} = \sigma([W_{fx}, U_{fh}] * [x^{(t)}, h^{(t-1)}] + b_f) \quad (15)$ $i^{(t)} = \sigma([W_{ix}, U_{ih}] * [x^{(t)}, h^{(t-1)}] + b_i) \quad (16)$ $o^{(t)} = \sigma([W_{ox}, U_{oh}] * [x^{(t)}, h^{(t-1)}] + b_o) \quad (17)$ $g^{(t)} = \tanh([W_{gx}, U_{gh}] * [x^{(t)}, h^{(t-1)}] + b_g) \quad (18)$ $c^{(t)} = f^{(t)} \odot c^{(t-1)} + i^{(t)} \odot g^{(t)} \quad (19)$ $h^{(t)} = \tanh(c^{(t)}) \odot o^{(t)} \quad (20)$
M2		$f^{(t)} = \sigma([W_{fx}, U_{fh}] * [x^{(t)}, h^{(t-1)}] + b_f) \quad (21)$ $g^{(t)} = \tanh([W_{gx}, U_{gh}] * [x^{(t)}, h^{(t-1)}] + b_g) \quad (22)$ $c^{(t)} = f^{(t)} \odot c^{(t-1)} + g^{(t)} \quad (23)$ $h^{(t)} = \tanh(c^{(t)}) \quad (24)$
M3		$f^{(t)} = \sigma([W_{fx}, U_{fh}] * [x^{(t)}, h^{(t-1)}] + b_f) \quad (25)$ $i^{(t)} = \sigma([W_{ix}, +U_{ih}] * [x^{(t)}, h^{(t-1)}] + b_i) \quad (26)$ $g^{(t)} = \tanh([W_{gx}, U_{gh}] * [x^{(t)}, h^{(t-1)}] + b_g) \quad (27)$ $c^{(t)} = f^{(t)} \odot c^{(t-1)} + i^{(t)} \odot g^{(t)} \quad (28)$ $h^{(t)} = \tanh(c^{(t)}) \quad (29)$
M4		$f^{(t)} = \sigma([W_{fx}, U_{fh}] * [x^{(t)}, h^{(t-1)}] + b_f) \quad (30)$ $o^{(t)} = \sigma([W_{ox}, U_{oh}] * [x^{(t)}, h^{(t-1)}] + b_o) \quad (31)$ $g^{(t)} = \tanh([W_{gx}, U_{gh}] * [x^{(t)}, h^{(t-1)}] + b_g) \quad (32)$ $c^{(t)} = f^{(t)} \odot c^{(t-1)} + i^{(t)} \odot g^{(t)} \quad (33)$ $h^{(t)} = \tanh(c^{(t)}) \odot o^{(t)} \quad (34)$

M5



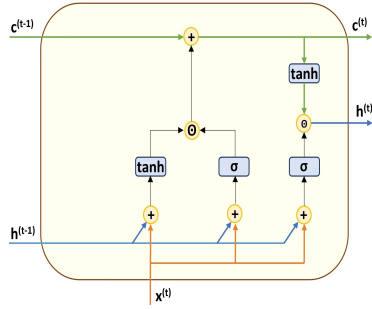
$$i^{(t)} = \sigma([W_{ix}, U_{ih}] * [x^{(t)}, h^{(t-1)}] + b_i) \quad (35)$$

$$g^{(t)} = \tanh([W_{gx}, U_{gh}] * [x^{(t)}, h^{(t-1)}] + b_g) \quad (36)$$

$$c^{(t)} = c^{(t-1)} + i^{(t)} \odot g^{(t)} \quad (37)$$

$$h^{(t)} = \tanh(c^{(t)}) \quad (38)$$

M6



$$i^{(t)} = \sigma([W_{ix}, U_{ih}] * [x^{(t)}, h^{(t-1)}] + b_i) \quad (39)$$

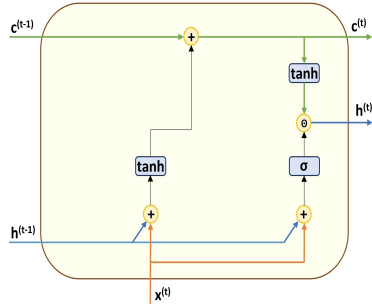
$$o^{(t)} = \sigma([W_{ox}, U_{oh}] * [x^{(t)}, h^{(t-1)}] + b_o) \quad (40)$$

$$g^{(t)} = \tanh([W_{gx}, U_{gh}] * [x^{(t)}, h^{(t-1)}] + b_g) \quad (41)$$

$$c^{(t)} = c^{(t-1)} + i^{(t)} \odot g^{(t)} \quad (42)$$

$$h^{(t)} = \tanh(c^{(t)}) \odot o^{(t)} \quad (43)$$

M7



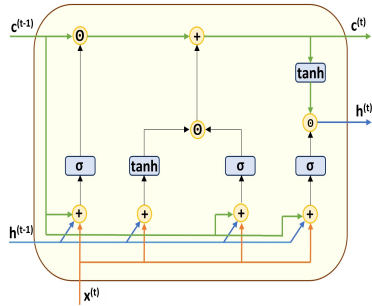
$$o^{(t)} = \sigma([W_{ox}, U_{oh}] * [x^{(t)}, h^{(t-1)}] + b_o) \quad (44)$$

$$g^{(t)} = \tanh([W_{gx}, U_{gh}] * [x^{(t)}, h^{(t-1)}] + b_g) \quad (45)$$

$$c^{(t)} = c^{(t-1)} + i^{(t)} \odot g^{(t)} \quad (46)$$

$$h^{(t)} = \tanh(c^{(t)}) \odot o^{(t)} \quad (47)$$

M8



$$f^{(t)} = \sigma([W_{fx}, U_{fh}, W_{fc}] * [x^{(t)}, h^{(t-1)}, c^{(t-1)}] + b_f) \quad (48)$$

$$i^{(t)} = \sigma([W_{ix}, U_{ih}, W_{ic}] * [x^{(t)}, h^{(t-1)}, c^{(t-1)}] + b_i) \quad (49)$$

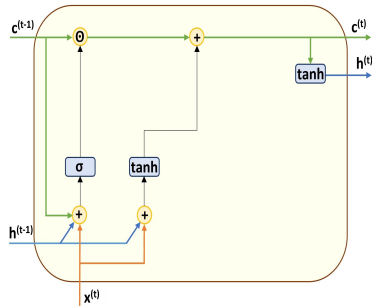
$$o^{(t)} = \sigma([W_{ox}, U_{oh}, W_{oc}] * [x^{(t)}, h^{(t-1)}, c^{(t-1)}] + b_o) \quad (50)$$

$$g^{(t)} = \tanh([W_{gx}, U_{gh}] * [x^{(t)}, h^{(t-1)}] + b_g) \quad (51)$$

$$c^{(t)} = f^{(t)} \odot c^{(t-1)} + i^{(t)} \odot g^{(t)} \quad (52)$$

$$h^{(t)} = \tanh(c^{(t)}) \odot o^{(t)} \quad (53)$$

M9



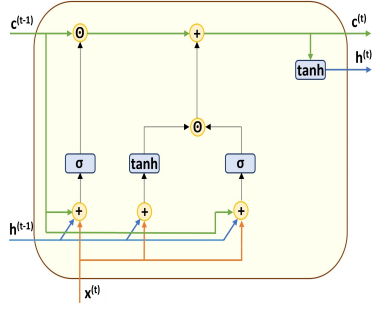
$$f^{(t)} = \sigma([W_{fx}, U_{fh}, W_{fc}] * [x^{(t)}, h^{(t-1)}, c^{(t-1)}] + b_f) \quad (54)$$

$$g^{(t)} = \tanh([W_{gx}, U_{gh}] * [x^{(t)}, h^{(t-1)}] + b_g) \quad (55)$$

$$c^{(t)} = f^{(t)} \odot c^{(t-1)} + g^{(t)} \quad (56)$$

$$h^{(t)} = \tanh(c^{(t)}) \quad (57)$$

M10



$$f^{(t)} = \sigma([W_{fx}, U_{fh}, W_{fc}] * [x^{(t)}, h^{(t-1)}, c^{(t-1)}] + b_f) \quad (58)$$

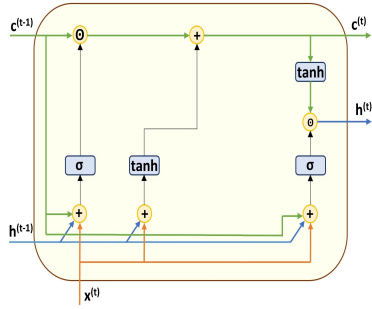
$$i^{(t)} = \sigma([W_{ix}, U_{ih}, W_{ic}] * [x^{(t)}, h^{(t-1)}, c^{(t-1)}] + b_i) \quad (59)$$

$$g^{(t)} = \tanh([W_{gx}, U_{gh}] * [x^{(t)}, h^{(t-1)}] + b_g) \quad (60)$$

$$c^{(t)} = f^{(t)} \odot c^{(t-1)} + i^{(t)} \odot g^{(t)} \quad (61)$$

$$h^{(t)} = \tanh(c^{(t)}) \quad (62)$$

M11



$$f^{(t)} = \sigma([W_{fx}, U_{fh}, W_{fc}] * [x^{(t)}, h^{(t-1)}, c^{(t-1)}] + b_f) \quad (63)$$

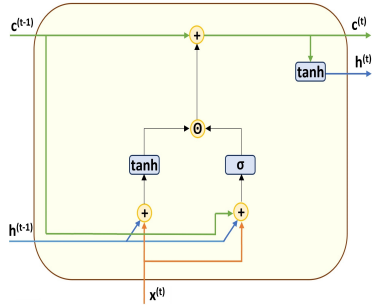
$$o^{(t)} = \sigma([W_{ox}, U_{oh}, W_{oc}] * [x^{(t)}, h^{(t-1)}, c^{(t-1)}] + b_o) \quad (64)$$

$$g^{(t)} = \tanh([W_{gx}, U_{gh}] * [x^{(t)}, h^{(t-1)}] + b_g) \quad (65)$$

$$c^{(t)} = f^{(t)} \odot c^{(t-1)} + g^{(t)} \quad (66)$$

$$h^{(t)} = \tanh(c^{(t)}) \odot o^{(t)} \quad (67)$$

M12



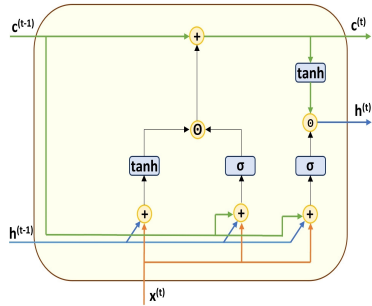
$$i^{(t)} = \sigma([W_{ix}, U_{ih}, W_{ic}] * [x^{(t)}, h^{(t-1)}, c^{(t-1)}] + b_i) \quad (68)$$

$$g^{(t)} = \sigma([W_{gx}, U_{gh}] * [x^{(t)}, h^{(t-1)}] + b_g) \quad (69)$$

$$c^{(t)} = c^{(t-1)} + i^{(t)} \odot g^{(t)} \quad (70)$$

$$h^{(t)} = \tanh(c^{(t)}) \quad (71)$$

M13



$$i^{(t)} = \sigma([W_{ix}, U_{ih}, W_{ic}] * [x^{(t)}, h^{(t-1)}, c^{(t-1)}] + b_i) \quad (72)$$

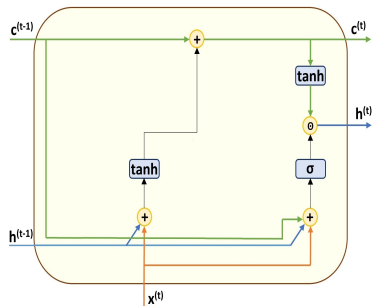
$$o^{(t)} = \sigma([W_{ox}, U_{oh}, W_{oc}] * [x^{(t)}, h^{(t-1)}, c^{(t-1)}] + b_o) \quad (73)$$

$$g^{(t)} = \tanh([W_{gx}, U_{gh}] * [x^{(t)}, h^{(t-1)}] + b_g) \quad (74)$$

$$c^{(t)} = c^{(t-1)} + i^{(t)} \odot g^{(t)} \quad (75)$$

$$h^{(t)} = \tanh(c^{(t)}) \odot o^{(t)} \quad (76)$$

M14



$$o^{(t)} = \sigma([W_{ox}, U_{oh}, W_{oc}] * [x^{(t)}, h^{(t-1)}, c^{(t-1)}] + b_o) \quad (77)$$

$$g^{(t)} = \tanh([W_{gx}, U_{gh}] * [x^{(t)}, h^{(t-1)}] + b_g) \quad (78)$$

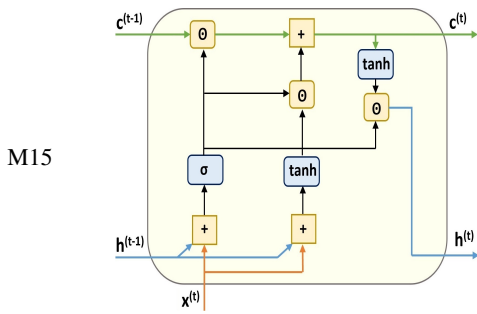
$$c^{(t)} = c^{(t-1)} + i^{(t)} \odot g^{(t)} \quad (79)$$

$$h^{(t)} = \tanh(c^{(t)}) \odot o^{(t)} \quad (80)$$

TABLE 20 The six multi-function gate variants of convolution LSTM-based models. M15 is an alias for the np-rgcLSTM and M18 is an alias for the rgcLSTM.

Model *Diagram*

Formulas

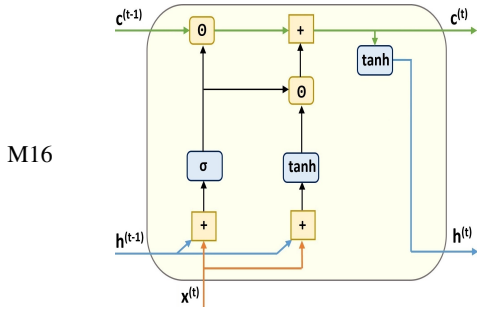


$$f^{(t)} = \sigma([W_{fx}, U_{fh}] * [x^{(t)}, h^{(t-1)}] + b_f) \quad (81)$$

$$g^{(t)} = \tanh([W_{gx}, U_{gh}] * [x^{(t)}, h^{(t-1)}] + b_g) \quad (82)$$

$$c^{(t)} = f^{(t)} \odot c^{(t-1)} + f^{(t)} \odot g^{(t)} \quad (83)$$

$$h^{(t)} = \tanh(c^{(t)}) \odot f^{(t)} \quad (84)$$

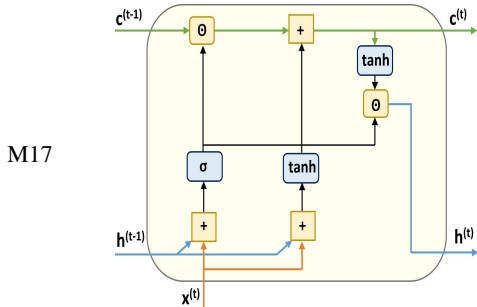


$$f^{(t)} = \sigma([W_{fx}, U_{fh}] * [x^{(t)}, h^{(t-1)}] + b_f) \quad (85)$$

$$g^{(t)} = \tanh([W_{gx}, U_{gh}] * [x^{(t)}, h^{(t-1)}] + b_g) \quad (86)$$

$$c^{(t)} = f^{(t)} \odot c^{(t-1)} + f^{(t)} \odot g^{(t)} \quad (87)$$

$$h^{(t)} = \tanh(c^{(t)}) \quad (88)$$

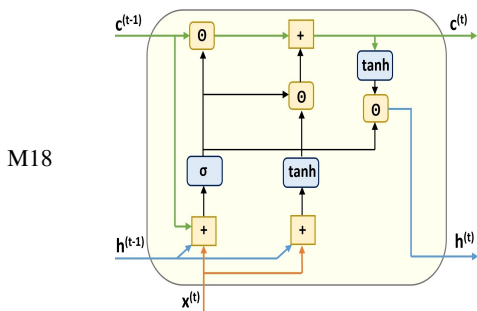


$$f^{(t)} = \sigma([W_{fx}, U_{fh}] * [x^{(t)}, h^{(t-1)}] + b_f) \quad (89)$$

$$g^{(t)} = \tanh([W_{gx}, U_{gh}] * [x^{(t)}, h^{(t-1)}] + b_g) \quad (90)$$

$$c^{(t)} = f^{(t)} \odot c^{(t-1)} + g^{(t)} \quad (91)$$

$$h^{(t)} = \tanh(c^{(t)}) \odot f^{(t)} \quad (92)$$

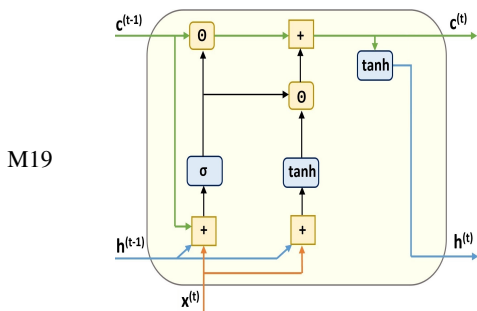


$$f^{(t)} = \sigma([W_{fx}, U_{fh}, W_{fc}] * [x^{(t)}, h^{(t-1)}, c^{(t-1)}] + b_f) \quad (93)$$

$$g^{(t)} = \tanh([W_{gx}, U_{gh}] * [x^{(t)}, h^{(t-1)}] + b_g) \quad (94)$$

$$c^{(t)} = f^{(t)} \odot c^{(t-1)} + f^{(t)} \odot g^{(t)} \quad (95)$$

$$h^{(t)} = \tanh(c^{(t)}) \odot f^{(t)} \quad (96)$$

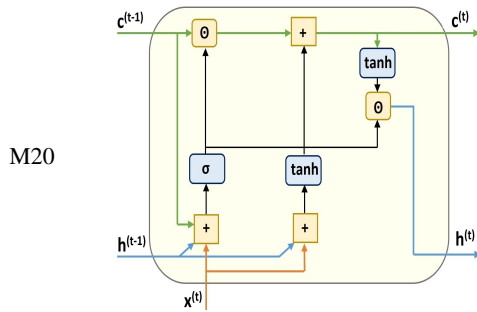


$$f^{(t)} = \sigma([W_{fx}, U_{fh}, W_{fc}] * [x^{(t)}, h^{(t-1)}, c^{(t-1)}] + b_f) \quad (97)$$

$$g^{(t)} = \tanh([W_{gx}, U_{gh}] * [x^{(t)}, h^{(t-1)}] + b_g) \quad (98)$$

$$c^{(t)} = f^{(t)} \odot c^{(t-1)} + f^{(t)} \odot g^{(t)} \quad (99)$$

$$h^{(t)} = \tanh(c^{(t)}) \quad (100)$$



$$f^{(t)} = \sigma([W_{fx}, U_{fh}, W_{fc}] * [x^{(t)}, h^{(t-1)}, c^{(t-1)}] + b_f) \quad (101)$$

$$g^{(t)} = \tanh([W_{gx}, U_{gh}] * [x^{(t)}, h^{(t-1)}] + b_g) \quad (102)$$

$$c^{(t)} = f^{(t)} \odot c^{(t-1)} + g^{(t)} \quad (103)$$

$$h^{(t)} = \tanh(c^{(t)}) \odot f^{(t)} \quad (104)$$

References

1. Friston Karl. A Theory of Cortical Responses. *Phil. Trans. R. Soc. B.* 2005;360:815-836.
2. Bastos A., Usrey W., Adams R., Mangun G., Fries P., Friston K. Canonical Microcircuits for Predictive Coding. *Neuron.* 2012;76(4):695–711.
3. Rao R., Ballard D.. Predictive Coding in the Visual Cortex: a Functional Interpretation of some Extra-Classical Receptive-Field Effects. *Nature Neuroscience.* 1999;2(1):79.
4. Lotter W., Kreiman G., Cox D.. Deep Predictive Coding Networks for Video Prediction and Unsupervised Learning. In: International Conference on Learning Representations; 2017.
5. Chollet François et al. Keras: The Python Deep Learning Library. <https://keras.io/>, 2015.
6. Paszke A., Gross S., Chintala S., et al. Automatic Differentiation in PyTorch. In: NIPS 2017 Workshop Autodiff; 2017.
7. Martin A., Agarwal A., Barham P., et al. *TensorFlow: Large-Scale Machine Learning on Heterogeneous Systems.* <https://www.tensorflow.org/>; 2015.
8. Shi X., Chen Z., Wang H., Yueng D., Wong W., Woo W. Convolutional LSTM Network: A Machine Learning Approach for Precipitation Nowcasting. *Advances in Neural Information Processing Systems.* 2015;28:802-810.
9. Sohn H., Farrar C.. Damage Diagnosis using Time Series Analysis of Vibration Signals. *Smart Materials and Structures.* 2001;10(3):446.
10. Rotton J., Frey J. Air Pollution, Weather, and Violent Crimes: Concomitant Time-Series Analysis of Archival Data. *Journal of Personality and Social Psychology.* 1985;49(5):1207.
11. Elsayed N., Maida A., Bayoumi M.. Deep Gated Recurrent and Convolutional Network Hybrid Model for Univariate Time Series Classification. *arXiv preprint arXiv:1812.07683.* 2018;.
12. Srivastava N., Mansimov E., Salakhudinov R. Unsupervised Learning of Video Representations using LSTMs. *International Conference on Machine Learning.* 2015;:843–852.
13. Finn C., Goodfellow I., Levine S.. Unsupervised Learning for Physical Interaction through Video Prediction. *Advances in Neural Information Processing Systems.* 2016;:64–72.
14. Hochreiter Sepp, Schmidhuber Jürgen. Long Short-Term Memory. *Neural Computation.* 1997;9(8):1735-1780.
15. Greff K., Srivastava R., Koutník J., Steunebrink B., Schmidhuber J. LSTM: A Search Space Odyssey. *IEEE Transactions on Neural Networks and Learning Systems.* 2017;28(10):2222–2232.

16. Cho K., M. Van, Bahdanau D., Bengio Y. On the Properties of Neural Machine Translation: Encoder-Decoder Approaches. *arXiv preprint arXiv:1409.1259*. 2014;.
17. Zhou G., Wu J., Zhang C., Zhou Z.. Minimal Gated Unit for Recurrent Neural Networks. *International Journal of Automation and Computing*. 2016;13(3):226–234.
18. Chung J., Gulcehre C., Cho K., Bengio Y. Empirical Evaluation of Gated Recurrent Neural Networks on Sequence Modeling. *arXiv preprint arXiv:1412.3555*. 2014;.
19. Gers F., Schmidhuber J., Cummins F.. Learning to Forget: Continual Prediction with LSTM. *Neural Computation*. 2000;:2451-2471.
20. Heck J., Salem F. Simplified Minimal Gated Unit Variations for Recurrent Neural Networks. *arXiv preprint arXiv:1701.03452*. 2017;.
21. Jozefowicz R., Zaremba W., Sutskever I.. An Empirical Exploration of Recurrent Network Architectures. *International Conference on Machine Learning*. 2015;:2342–2350.
22. Gulcehre C., Moczulski M., Denil M., Bengio Y.. Noisy Activation Functions. *International Conference on Machine Learning*. 2016;:3059-3068.
23. Elsayed N., Maida A., Bayoumi M.. Reduced-Gate Convolutional LSTM Architecture for Next-Frame Video Prediction Using Predictive Coding. *2019 International Joint Conference on Neural Networks (IJCNN)*. 2019;:1-9.
24. Elsayed N., Maida A., Bayoumi M. Empirical Activation Function Effects on Unsupervised Convolutional LSTM Learning. *2018 IEEE 30th International Conference on Tools with Artificial Intelligence (ICTAI)*. 2018;:336–343.
25. Elsayed N., Maida A., Bayoumi M. Effects of Different Activation Functions for Unsupervised Convolutional LSTM Spatiotemporal Learning. *Advances in Science, Technology and Engineering Systems Journal*. 2019;4(2):260–269.
26. Geiger A., Lenz P., Stiller C., Urtasun R.. Vision Meets Robotics: The KITTI Dataset. *The International Journal of Robotics Research*. 2013;32(11):1231–1237.
27. Kingma D., Ba J.. Adam: A Method for Stochastic Optimization. *arXiv preprint arXiv:1412.6980*. 2014;.
28. Gers F., Schraudolph N., Schmidhuber J.. Learning Precise Timing with LSTM Recurrent Networks. *Journal of Machine Learning Research*. 2002;3:115–143.
29. Wang Y., Gao Z., Long M., Wang J., Yu P. PredRNN++: Towards A Resolution of the Deep-in-Time Dilemma in Spatiotemporal Predictive Learning. *arXiv preprint arXiv:1804.06300*. 2018;.
30. Jia X., De Brabandere B., Tuytelaars T., Gool L.. Dynamic Filter Networks. *Advances in Neural Information Processing Systems*. 2016;29:667–675.
31. Kalchbrenner N., Oord A., Simonyan K., et al. Video Pixel Networks. *arXiv preprint arXiv:1610.00527*. 2016;.
32. Shi X., Gao Z., Lausen L., et al. Deep Learning for Precipitation Nowcasting: A Benchmark and a New Model. *Advances in Neural Information Processing Systems*. 2017;30:5617–5627.
33. Wang Y., Long M., Wang J., Gao Z., Philip S. Y. PredRNN: Recurrent Neural Networks for Predictive Learning using Spatiotemporal LSTMs. *Advances in Neural Information Processing Systems*. 2017;:879–888.
34. Wang Z., Bovik A. C, Sheikh H. R., Simoncelli E. P. Image Quality Assessment: From Error Visibility to Structural Similarity. *IEEE Transactions on Image Processing*. 2004;13(4):600–612.

AUTHOR BIOGRAPHY



Nelly ELSayed is an assistant professor at the School of Information Technology, University of Cincinnati. She received her Bachelor degree in Computer Science from Alexandria University in 2010 and she was ranked the First on Computer Science Class. She received two Master degrees, the first in Computer Science in 2014 at Alexandria University and the second in Computer Engineering in 2017 from the University of Louisiana at Lafayette. She received her Ph.D. in Computer Engineering from the University of Louisiana at Lafayette. She is an honor member in the national society of leadership and the honor society Phi Kappa Phi. Her major research interests are in machine learning, artificial intelligence, convolutional recurrent neural networks, bio-inspired computations, information technology, data science, and data analysis.



Anthony S. Maida is associate professor, Alfred and Helen M. Lamson Endowed Professor in computer science, and graduate coordinator for computer science and computer engineering at School of Computing and Informatics, University of Louisiana at Lafayette. He received this BA in Mathematics in 1973, Ph.D. in Psychology in 1980, and Masters Degree in Computer Science in 1981, all from the University of Buffalo. He has done two Post Doctoral degrees at Brown University and the University of California, Berkeley. He was a member of the computer science faculty at the Penn State University from 1984 through 1991. He has been a member of a Center for Advanced Computer Studies and School of Computing and informatics at the University of Louisiana at Lafayette from 1991 to the present. His research interests are: intelligent systems, neural networks, recurrent neural networks and brain simulation.



Magdy Bayoumi is department head and professor at the Electrical Engineering Department, University of Louisiana at Lafayette. He was the Director of CACS, 1997 to 2013 and Department Head of the Computer Science Department, 2000-2011. Dr. Bayoumi has been a faculty member in CACS since 1985. He received B.Sc. and M.Sc. degrees in Electrical Engineering from Cairo University, Egypt; M.Sc. degree in Computer Engineering from Washington University, St. Louis; and Ph.D. degree in Electrical Engineering from the University of Windsor, Canada. He is on the IEEE Fellow Committee and he was on the IEEE CS Fellow Committee. His research interests are: technology, data processing, management, internet of things, energy and security.

